Article:
Garum, M, Glover, PWJ, Lorinczi, P et al. (2020) Micro- and Nano-Scale Pore Structure in Gas Shale Using Xμ-CT and FIB-SEM Techniques. Energy & Fuels, 34 (10). pp. 12340-12353. ISSN: 0887-0624

https://doi.org/10.1021/acs.energyfuels.0c02025

Micro- and nano-scale pore structure in gas shale using Xμ-CT and FIB-SEM techniques

Mohamed Garum[1], Paul W.J. Glover[2], Piroska Lorinczi[2], Rik Drummond-Brydson[1], Ali Hassanpour[1*]

[1]School of Chemical and Process Engineering, University of Leeds, Leeds LS2 9JT, U.K.

[2]School of Earth and Environment, University of Leeds, Leeds LS2 9JT, U.K.

*Corresponding author (A.H.): Tel: +44(0)113 343 2405; Email: A.Hassanpour@leeds.ac.uk

Abstract

Shale is a complex rock composed of a complex mixture of matrix minerals, kerogen and having a complex pore microstructure. The pore microstructure is highly-dependent upon the scale at which it is considered. Such microstructure is important for the assessment of the potential of gas shales based on the connectivity and pores at each scale, and the ability of the rock to be hydraulically fractured. In this work the three dimensional (3D) structure of Bowland shale has been investigated at both microscopic and nanoscopic scales on the same sample for the first time using (i) a combination of serial sectioning, using focused ion beam (FIB) milling and scanning electron microscopy (SEM), and (ii) X-ray micro-computed tomography (Xμ-CT). The reconstructed matrix, kerogen and pore space volumes from each approach showed significant scale-dependent differences in microstructure. The shale samples displayed a high kerogen content with high connectivity. Porosity in the shale rock sample was observed to be prevalent in either the inorganic matrix, the kerogen, or both. Furthermore, the porosity from the reconstructed shale volumes was found to vary with location, as sampled by FIB-SEM, within the shale samples taken for Xμ-CT. Pore volume, scale invariant surface area to volume ratio and two orthogonal pore aspect ratio distributions were extracted from the reconstructed image data by 3D image analysis. These data show that voids within the rock are oblate at all scales. However, the smaller pores visible by FIB-SEM present higher scale invariant surface area to volume ratios, indicating that they are more likely to interlink the larger pores visible by Xμ-CT and form a small scale but highly connected pore network for fluid flow. Permeabilities have been calculated from both the FIB-SEM and Xμ-CT images and fall in the range 2.98 nD to 150 nD, broadly agreeing with experimental determinations from another author.

Keywords. Gas shale, FIB-SEM, Xμ-CT, porosity, permeability, Kerogen, pore volume, size distribution, pore aspect ratio and surface area to pore volume.

---

1. Introduction

The increasing demand of the hydrocarbons as an energy source has led to the investigation of gas shale resources [1]. Between 2010 and 2020 there was an approximately threefold increase in known reserves of shale gas worldwide [2]; in the USA alone proven reserves reached 9 x 10^{12} m^3 [3].

The commercial success in shale gas production in the USA has been achieved largely due to advances in completion and drilling technologies [4] such as hydraulic fracturing and horizontal drilling. Shale has extremely low permeability, which is its main exploitation

challenge. Consequently, having a better understanding of how its microstructures control both porosity and permeability would be hugely beneficial. Such knowledge would increase our capacity to identify sources and extract shale gas more efficiently at lower costs. For example, the wettability of the shale is largely controlled by the distribution of pores, in both of the organic and inorganic materials [5]. In addition, as pore sizes are reduced the physics of the fluid flow changes and the classic Darcy's law, as it stands, is no longer adequate to define the fluid flow. Moreover, pores in shales that are only a few nanometers in diameter could have significant adsorbed gas content as compared to their free gas content [5]. The pore shape is another significant physical parameter; round pores are much less prone to collapse from an external pressure than large aspect ratio, crack-like pores [6]. However, by contrast, large aspect ratio pores provide a higher surface area to volume ratio, which promotes gas desorption, compared to more spherical, low aspect ratio pores [4].

Understanding the pore structure of kerogen within gas shale is also important, as this is the potential source of the gas. Kerogen is the sedimentary organic matter (OM) which generates petroleum and natural gas and is commonly defined as the insoluble macromolecular species within the organic matter (OM) dispersed in sedimentary rocks [7]. It is believed that the pore structure of kerogen is controlled by micropores [8, 9], with lesser amounts of meso- and macropores [10].

Many techniques have been used to quantify the pore structure within the shale gas rocks. Amongst them, Mercury Injection Capillary Pressure (MICP) is a common method which involves forcing mercury (Hg) into the shale pores at high pressure and measuring the amount of Hg intrusion [11]. While extremely useful for high porosity clastic and carbonate rocks, the MICP technique is inappropriate for use with gas shales [12]. This is because gas shales have very low permeability, and mercury is a non-wetting phase. Extremely high pressures are required to force mercury into even the largest of the pores, and these pressures are large enough to compress the rock sample and perhaps damage the pores. Consequently, all pore size and porosity data provided by this technique is likely to be invalid for shale.

Focused Ion Beam Scanning Electron Microscopy (FIB-SEM) serial sectioning and X-ray Micro-Computed Tomography (Xμ-CT) have also been shown to be effective methods for the analysis and imaging of shale microstructure and porosity, and determining permeability. Both of these techniques reconstruct three-dimensional images of a small volume of a rock sample, providing data which can be analysed to give a wide range of characteristic parameters including porosity, pore size, pore shape, aspect ratios and surface to area volume ratios [6, 13]. However, each technique provides data over a different and overlapping range of scales, and with different resolutions [14]. The FIB-SEM approach provides data from about 5 nm to 10 μm, while the Xμ-CT technique covers the range of about 1 to 1000 μm.

At present, microscopic and nanoscopic data on shale characteristics is sparse, with 3D pore microstructure datasets available for only a relatively small number of different shales, and often only for some scale ranges. More experimental work is needed in order to fully understand the impact of heterogeneity, pore and kerogen distributions and their connectivity.

Ma et al. [15] have carried out the workflow to quantitatively assess the size, geometry, connectivity of pores and organic matter on the Bowland reservoir based on 3D X-ray computed tomography and serial block face scanning electron microscopy (SEM). They have implemented a multi-scale approach on different sizes of samples based on the field of view and spatial resolution which represent the maximum and minimum sizes of images at each scale. The results showed that the pores, organic matter and clay minerals can be observed at lower (nanoscopic) scale due to the small pixel sizes, while at large (mesoscopic) scale only the fractures and layer of sedimentary rock can be observed. It is not possible to separate the clay minerals, organic matter and pores at this scale.

Ma et al. [10] and others [5, 15, 16, 17] have suggested that the Xμ-CT and FIB-SEM techniques can be used for the characterization of the micro-heterogeneity of shale reservoirs. However, such multi-scale measurements have only been carried out by using different samples to examine different scales. These different samples may not represent the same rock microstructure, while differences in their preparation, though carried out by careful cutting, could still lead to differential damage of the samples in a way that cannot be predicted or taken into account. Recently, Ma et al. [18] followed a methodology for the characterisation of Haynesville-Bossier Shale using a multi-scale set of measurements on a single sample.

In this paper, we describe a methodology to characterise a single sample of rock at multiple scales with multiple techniques, and use it to characterise the Bowland Shale for the first time. In our case, we carry out Xμ-CT measurements on a sample at the native resolution of the technique, and use the same sample to make higher resolution FIB-SEM measurements at specific multiple locations, each of which have a smaller field of view. This approach has a number of advantages: (i) The damage which occurs when the main sample is prepared is common to all measurements, simplifying the problem of understanding which aspects of the measurements are native to the specimen and which are caused by preparation for all measurements, irrespective of scale, resolution and field of view. (ii) The high resolution FIB-SEM measurements can be made at specific locations chosen with the aid of the 3D Xμ-CT data to be either representative of the whole sample, or to investigate specific aspects of features occurring in the whole specimen. (iii) Sufficient FIB-SEM measurements can be made to ensure that their mean behaviour represents that measured by the Xμ-CT measurements, but at much higher resolution. Consequently, we are able to understand the relationships between the microscale and macroscale properties and the impact of heterogeneity, pore and kerogen distributions and their connectivity, while the sample is not disturbed by the preparation method for the microscale measurements (FIB-SEM).

2. Material and Methods

2.1 Rock samples and preparation

The gas shale samples used in this study were obtained from the Bowland formation, collected from a depth of 2.7 km in a gas shale resource in Lancashire, UK. At the time of the study this was the sole source of gas shale reservoir material available to us. However, the Bowland formation underlies the great majority of northern England and has been estimated to have a P50 total in-place gas resource estimate of 264 Tcf in its upper Bowland-Hodder unit. The upper unit is more prospective than its other units and has been shown to closely

resemble the prolific North American shale gas plays. However, the upper Bowland-Hodder unit differs from most of the North American shale gas plays in that the productive zones are thicker, being hundreds of feet thick.

This study uses two different high-resolution imaging techniques, each of which probes a different scale, in the attempt to cover a wider range of scales than would be possible with a single technique alone, and to examine the extent to which each technique observes microstructural features at different scales with the primary aim of understanding the petrophysical properties of the of Bowland shale, including porosity and the microstructural distribution of pore volume. Table 1 summarizes the field of view and resolution of the 3D images, together with some characteristics obtained from the images by 3D image analysis.

Table 1. Summary of the rocks and images studied in this paper.

Sample	Figures	Method (Location)	Image size (*x*×*y* pixel no.)	Voxel size (nm)	Measured Porosity (%)	Measured Kerogen (%)	Calculated Permeability (nD)
MD-2.7 km	3, 6	FIB-SEM (A)	3072×2048	20	0.10±0.01	34.8±1.74	13.85±3.45
MD-2.7 km	3, 6	FIB-SEM (B)	3072×2048	50	0.52±0.05	38.2±1.91	4.16±1.04
MD-2.7 km	3, 6	FIB-SEM (C)	3072×2048	50	0.94±0.09	41.4±2.07	150±37.5
MD-2.7 km	2	Xμ-CT	686×686	940	0.06±0.008	44.5±2.22	2.98±0.745

The two techniques we use in this work are 3D X-ray Micro-Computed Tomography scanning (Xμ-CT), and focused ion beam scanning electron microscopy (FIB-SEM), which uses a focused ion beam to successively strip material from the surface between scans. In our implementation, imaging has been possible with both techniques on a single quasi-cubic sample with a characteristic side length of about 500 μm. High resolution imaging, such as that carried out in this work requires very small samples, whose preparation is time-consuming and requires significant care. The higher the resolution we require, the smaller the samples must be. The following paragraph describes the preparation of such a sample.

In this work, samples were prepared by initially fine cutting a small sample of shale, followed by successive polishing of the sample's surfaces, as shown in Figure 1. In the first step, a thin layer was sliced from the parent sample using a diamond saw. That slice was sub-divided to produce cubes of side-length approximately 2 mm Figure 1a-b. In the second step (Figure 1c), each cube was mounted on a glass slide (26 mm × 48 mm) using thermo-plastic wax with a melting-point of between 80-85°C. During the third step each side of each sample was machined in turn to produce a cube of side length 0.5 mm. The machining was accomplished using a Buehler PetroThin® cutter/grinder (Figure 1d-e). After machining one side of the developing cube, the glass slide was again placed on the hotplate to melt the wax, allowing the sample to be turned in order to polish another face. After preparation, the sample was left attached to the slide to protect it, as shown in Figure 1f. The sample was only removed

from the slide and cleaned just before it was required for measurement. The cleaning was carried out using acetone machine to dissolve the wax under an optical microscope.

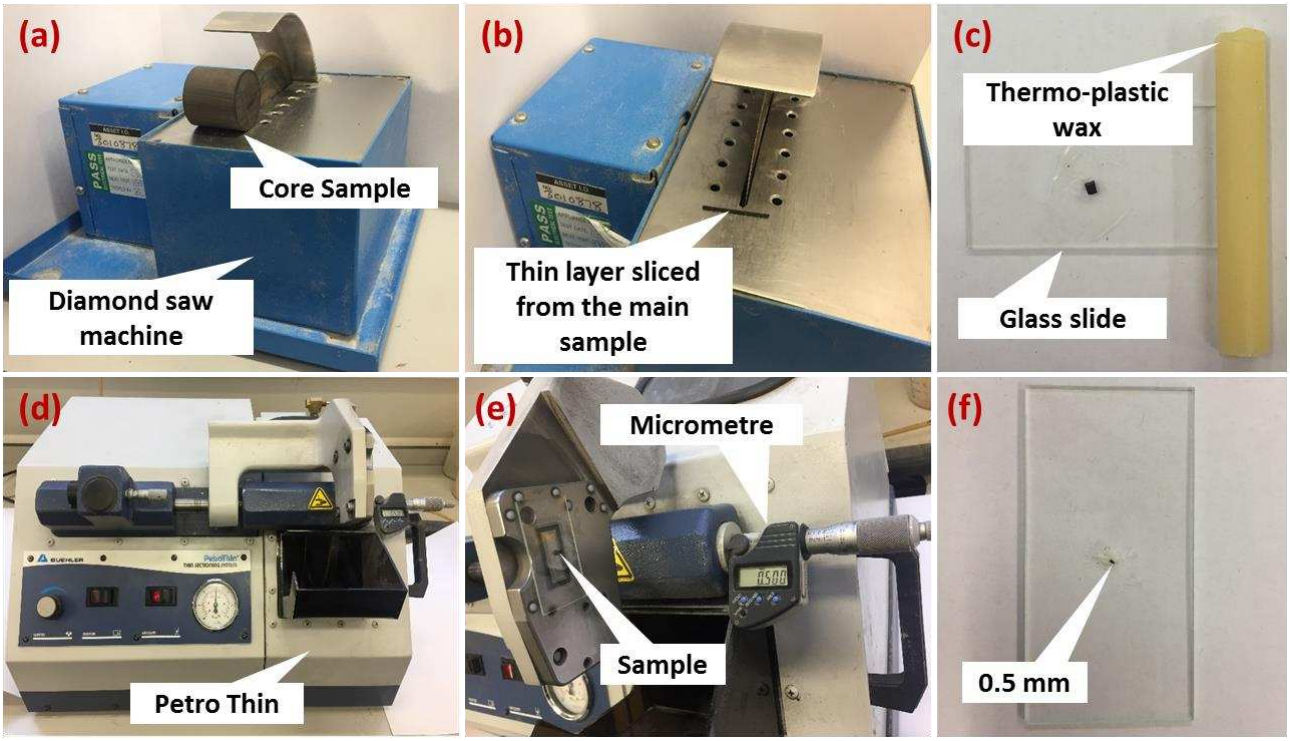

Figure 1. Illustration of the procedure of shale sample preparation. (a) Shale sample of around 4 mm using a diamond saw for cutting to slice cubes of length 2 mm. (b) A thin layer was sliced from the main sample and also using a diamond saw. (c) Glass slide and thermo-plastic wax used to hold the sample on the slide of the glass. (d) PetroThin® used for cutting, thin section of each side of shale. (e) The micrometer used to measure the size of shale. (f) A typical sample of size of around 500 µm attached to a glass slide with wax for transport.

2.2 Imaging Techniques

2.2.1 X-ray micro-CT

Modern X-ray micro-computed tomography (Xµ-CT) is a powerful non-destructive technique used for the materials characterization that provides 3D visualizations of the internal structure of the materials based on differential absorption of X-rays by the material [19]. A number of researchers have applied Xµ-CT to obtain visual representation of porosity and permeability for different materials, showing that this tool has the potential for being extremely useful in the oil and gas industries, enabling visualisation of the 3D distribution and connectivity of pores and the quantification of the relative amounts of mineral and organic matter [4, 13, 14, 20].

The Xµ-CT instrument used in this study was the Zeiss X-Radia 410 Versa. The X-ray source was operated at a voltage of 80 kV with a power of 7.0 W. The field of view (FOV) and pixel size was 928.4 µm and 0.94 µm, respectively, and is determined by the distances between

the X-ray source and the sample. Approximately 1000 slices were taken, each representing a 2D image, which when stacked forms the 3D imaged volume. The resulting voxel-size is 0.94×0.94×0.94 μm^3.

Figure 2 shows a Xμ-CT image of a part of a sample, superimposed on which are three selected locations (A, B and C) from which correlative FIB-SEM images and data were subsequently taken. In this figure, the three panels are the BSE-SEM images of the surface at these locations. Figure 3 shows a corresponding SEM image for the whole volume of the sample measured by Xμ-CT, again with three different locations A, B and C marked. Locations A and B were selected randomly, but to fulfil the criteria that they (i) did not contain significant observable iron pyrites, and (ii) otherwise the locations were not idiosyncratic. Location C was chosen to straddle the fracture that clearly crosses the sample. At the time of the choice it was unknown whether this fracture was part of the original structure of the rock, or was caused by sample preparation.

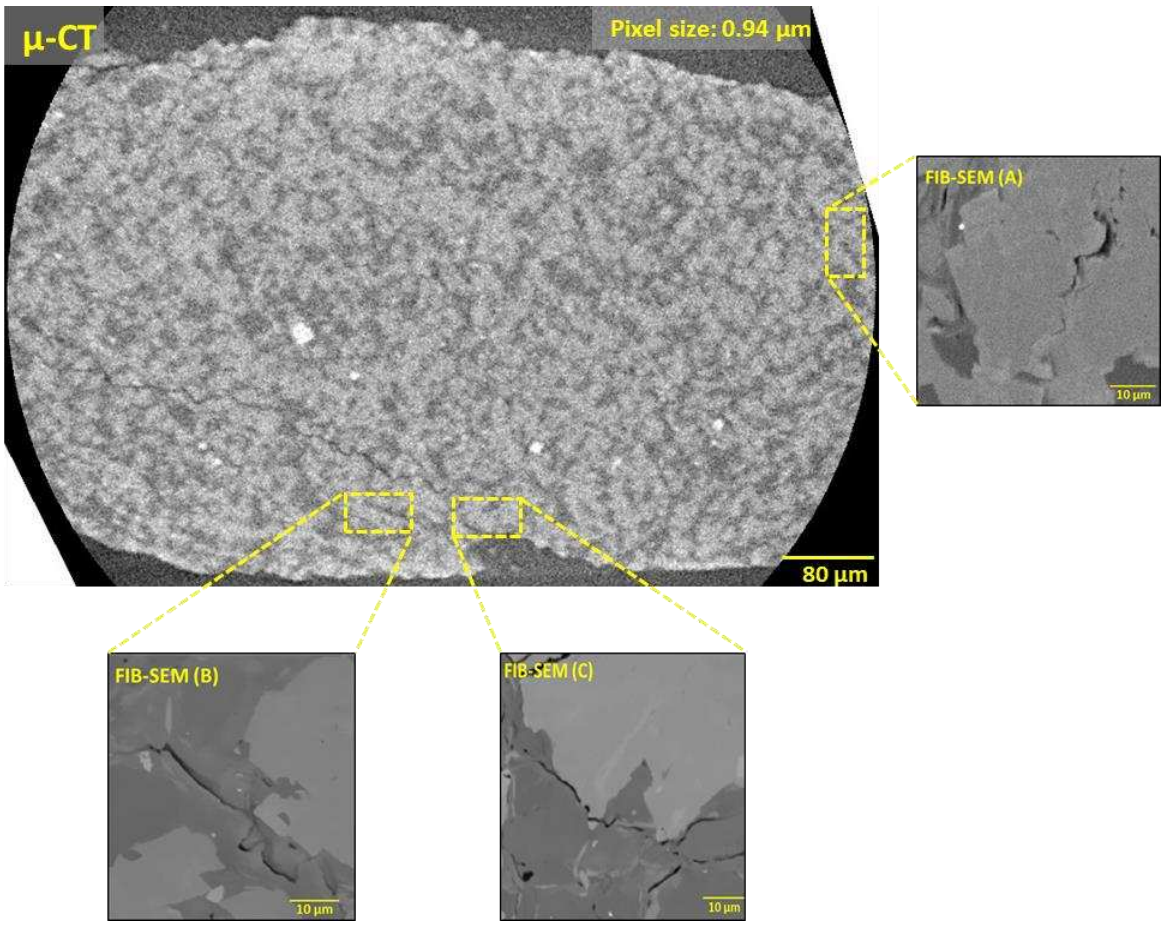

Figure 2. Xμ-CT image of sample MD-2.7 km of Bowland shale showing BSE images of a cross-section at each of the three locations A, B and C which were chosen for subsequent FIB-SEM serial sectioning.

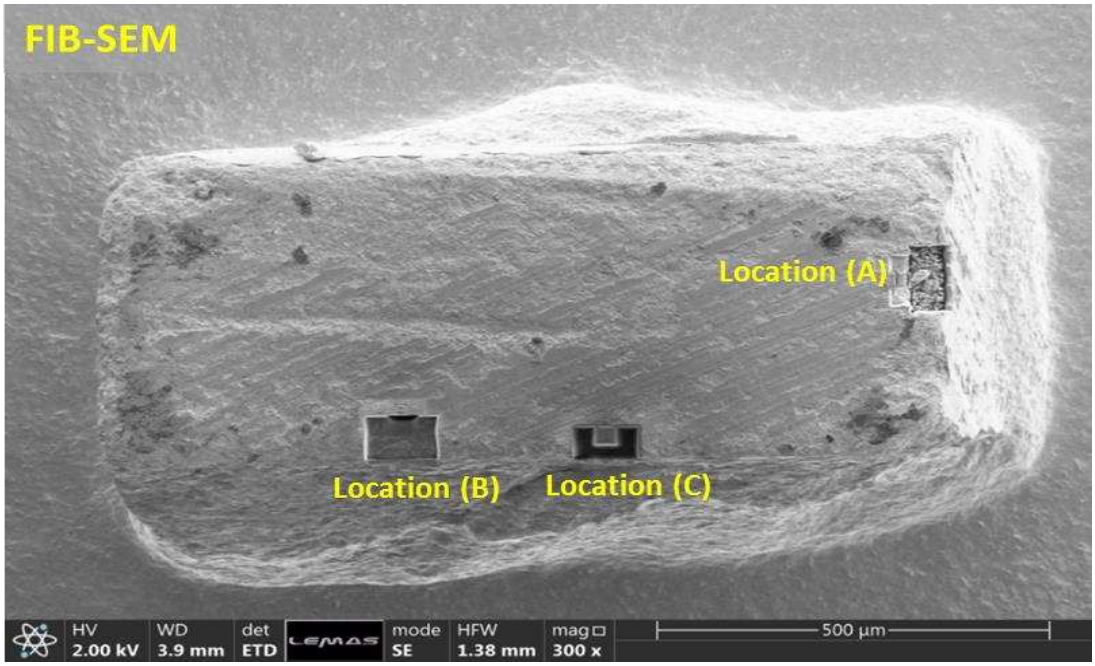

Figure 3. SEM image of the sample of Bowland shale used for Xμ-CT imaging showing the different locations A, B and C that were used for FIB-SEM serial sectioning.

2.2.2 Dual beam FIB-SEM

Scanning electron microscopy (SEM) has been an important technique for studying the nano- and micro-scale structures of pores in geosciences for many years. Imaging can be achieved using backscattered electrons (BSE) or secondary electrons (SE) as well as emitted X-rays for elemental analysis. Many authors have used SEM to produce images of gas shale microstructures [14, 21, 22, 23] but no comparative study of a variety of major shale gas samples has been performed to date.

For microstructural imaging of shale, preparation of the sample is of critical importance. Broken surfaces are inadequate as the rough texture of the shale surface makes the determination of the microstructural features unclear or ambiguous. Hand polished surfaces suffer from differential polishing due to the heterogeneous make-up of the shale [24]. Ion milled surfaces using broad ion beam (BIB) milling can produce good cross-sectional shale surfaces from large areas, however BIB ion-milling can produce undesired artefacts such as 'curtaining', which can make subsequent image analysis difficult. The relatively novel technique of Focused Ion Beam (FIB) milling allows site-specific cross-sectional investigation of features of interest at the micro-scale. The process of FIB milling provides a solution to these problems in terms of sample preparation and develop the cross-sectional preparation method in numerous arenas [25].

We have used a gallium ion beam milling FIB-SEM system (FEI Helios G4 CX DualBeam) which allows for the sample to be cross-sectioned and imaged *in-situ* using an integrated SEM. The FIB is set at a 52° angle to the vertical electron beam as shown in Figure 4. Initially the whole surface of the sample was coated with a conducting layer, Iridium was used and then a strip

of platinum is deposited onto the surface of the shale sample by ion-assisted deposition of a Pt ion-rich precursor gas. The protective layer dramatically decreases curtaining artefacts in the cross-sectioned shale surface [26]. Bulk material is then milled away using a 30 kV ion beam accelerating voltage and an 9.3 nA ion beam current in order to leave a small block of material, which will subsequently be serially sectioned (Figure 5). The cross-sectional face of the section was then gently milled using an ion beam voltage and current of 5 kV and 0.8 nA. The clean face of the sample exposed by this process can be imaged by the integrated SEM as a backscattered electron (BSE) image, as shown in Figure 5. Once imaging is completed, another layer of material can be removed by gentle FIB milling using the same parameters, before a second BSE image is acquired by the scanning electron microscope. On each occasion the FIB mills away a slice of material approximately 20 nm thick. Sequential milling and imaging effectively provides 3-D information about the shale microstructure. This milling and imaging process is repeated, typically 40-50 times, resulting in a 3D data set of SEM images with each image representing a 20 nm thick section of the shale. When combined with the lateral resolution of the scanning electron microscope images, the resulting voxel size for this technique is approximately 19x24x20 nm^3, making its resolution approximately 50 times greater than the Xμ-CT technique, described previously. In our implementation of the technique, the sample volume imaged was approximately 20x20x1 μm^3.

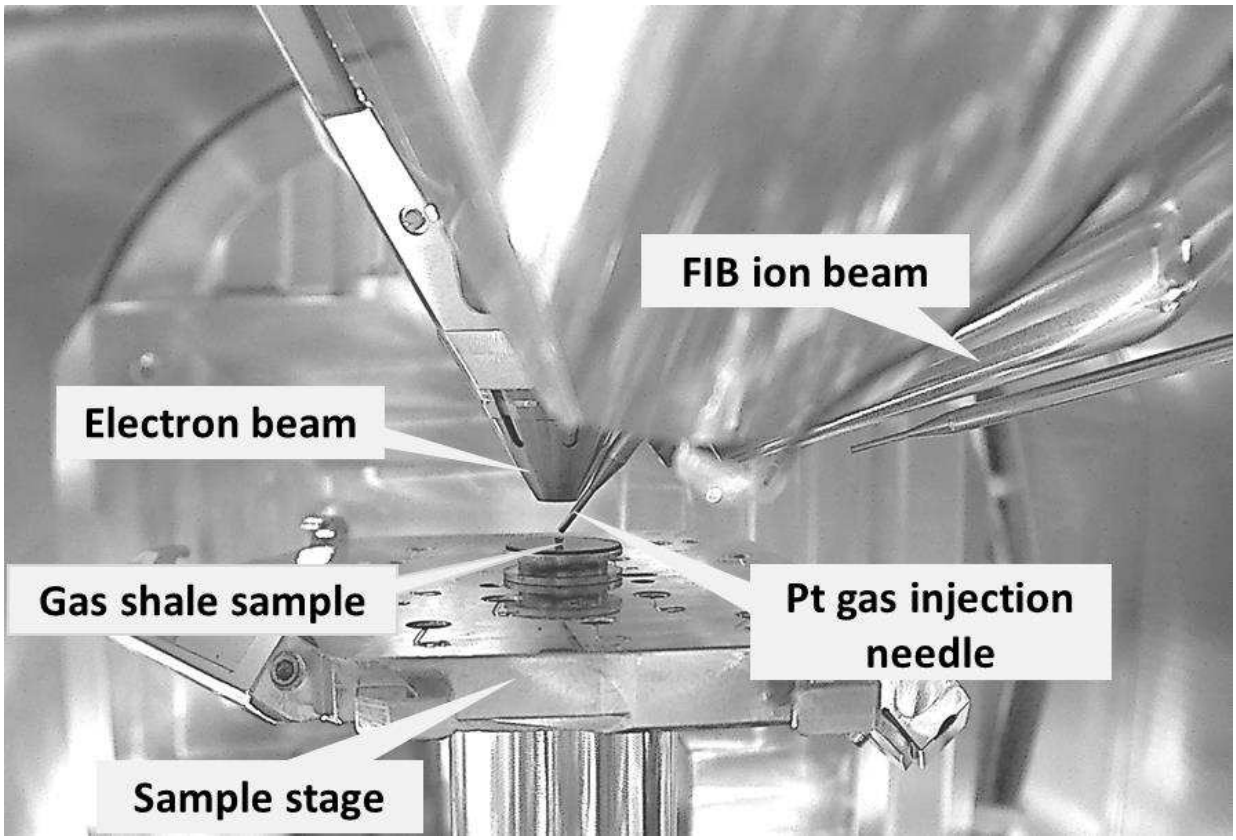

Figure 4. This FIB-SEM system consisting of an electron beam, FIB ion source (Ga), platinum (Pt) gas injection needle, sample stage and gas shale sample for analysis. The electron and ion beam were set at a 52° angle to each other.

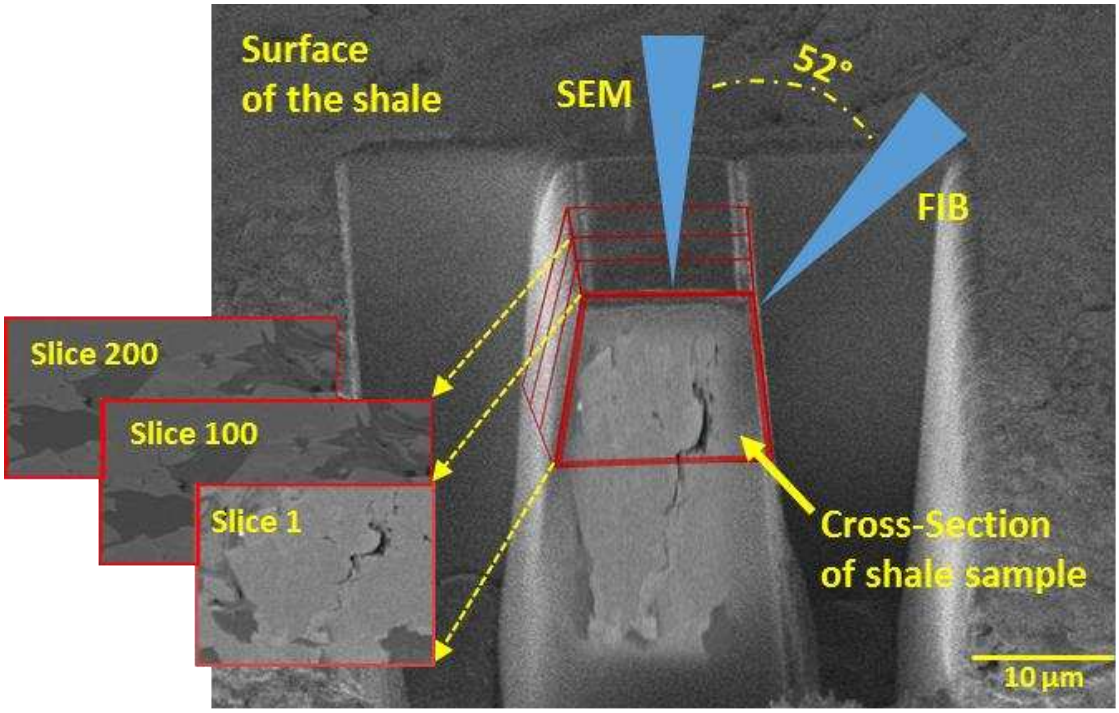

Figure 5. Serial cross-sectioning of a shale sample using a dual-beam FIB-SEM system. The ion beam is used to remove material from the shale surface creates a cross-sectional face that can be imaged by the electron beam.

Three separate locations (A, B and C) within the Xμ-CT sample were chosen for FIB-SEM analysis, as shown in Figures 2 and 3. Figure 6 shows BSE images of three separate regions A, B and C within samples taken from the same shale site prepared in cross-section. These images show significant differences in their microstructure and the size of their pores. Since the backscattered electron yield is sensitive to average atomic number, it provides means of differentiating the constituents of the microstructure dependent on whether they are composed of light or heavy elements. In Figure 6A, cracks (black) appear to be connected, while smaller dark areas (yellow circles) are isolated pores, which appear unconnected at the scale of the imaging, but may be connected at a finer scale. Kerogen appears as a lighter grey.

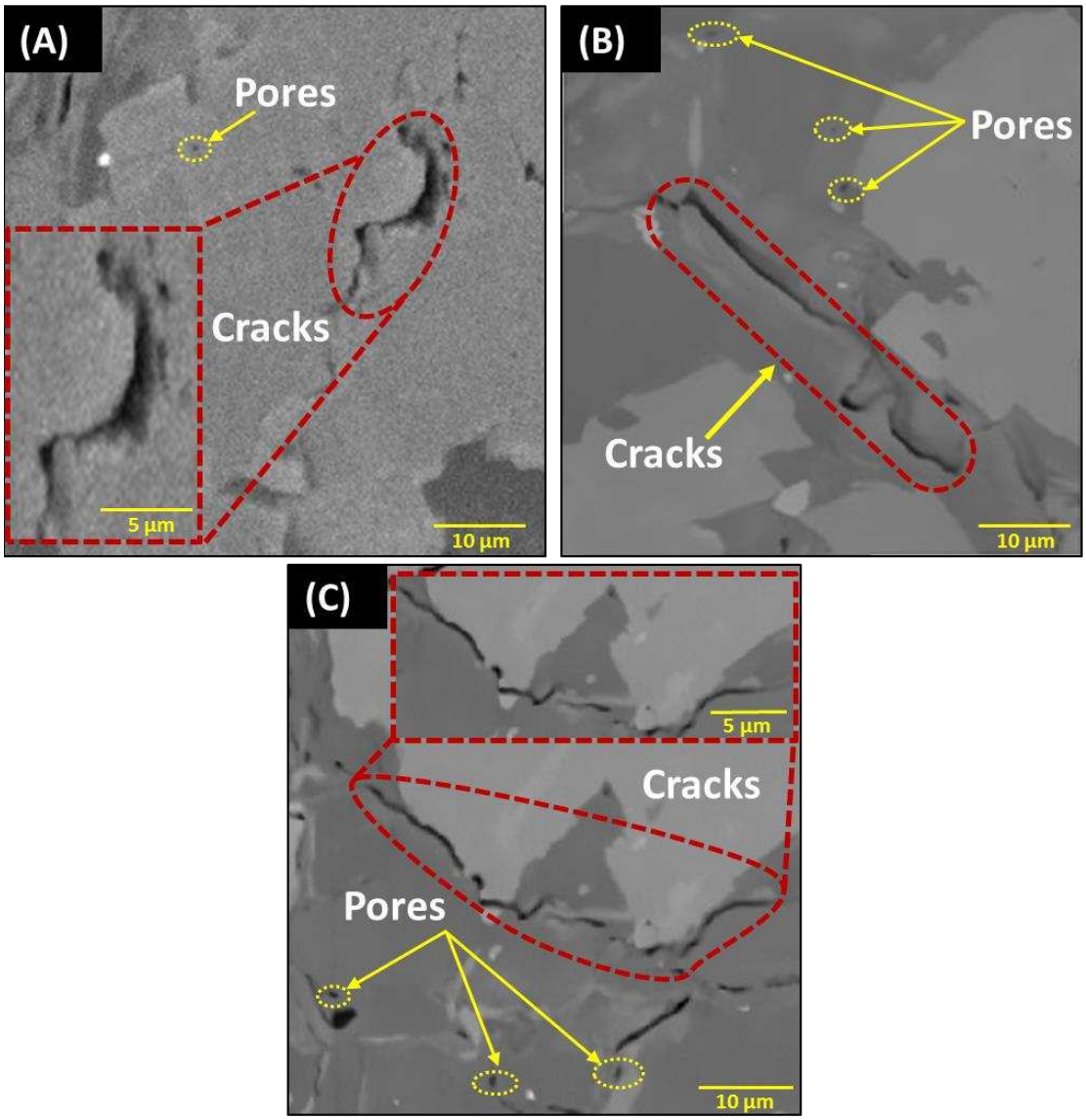

Figure 6. BSE images of FIB cross-sections taken from different locations A, B and C (see Figures 2 and 3), pores and cracks are highlighted by yellow and red circles.

2.3 Image processing

Image processing of the grey-scale 3D data volumes produced by Xμ-CT and FIB-SEM was carried out using the Avizo 9.0 software. This image processing was implemented in the following way. First, each 2D image from the dataset was aligned, cropped and filtered to reduce noise. In the second step, the 2D images were reconstructed in order to build a 3D dataset. The third step involved segmentation of the different phases on the basis of their greyscale values in order to distinguish between pores, kerogen, and matrix minerals [27, 28, 29]. Figure 7 shows the workflow and procedure of the analysis of the shale rock in this study. Once the samples had been fully filtered, reconstructed and segmented, the data was submitted to a range of image analysis procedures designed to measure a range of properties including pore volume, pore size, pore aspect ratios, the surface area to volume

ratio of pores, the three-dimensional orientation of pores and some measure of pore connectivity.

During the filtration step, a non-local means filter [30] was applied to both Xμ-CT and FIB-SEM images to remove noise without blurring the contrast between pores and the kerogen and also without decreasing resolution of the mineral phases, as shown in Figure 7b.

The greyscale images which arise from each of the techniques are 8-bit binary representations (0 to 255) of a measured physical property. In the case of Xμ-CT, they represent the CT number which is a proxy parameter that is sensitive to material density and atomic number. High value of greyscale, approaching 255 (i.e., light, high contrast regions), occur for lower density of the materials, while lower value, approaching 0 (darker regions represent high density). In the case of FIB-SEM, the greyscale images are also sensitive to atomic number and density, and once again the lighter regions represent denser and lower mean atomic number materials. Thus, in both images, pores appear as dark black region, while low mean atomic number materials such as pyrite appear as white regions; light black or light grey level regions correspond to medium density material which represents kerogen [31, 32]. There are many approaches to obtaining the thresholds between matrix minerals and kerogen, and between kerogen and open pore space [19, 27].

We have used the interactive and manual thresholding on each voxel based on the colour map [31, 33, 34]. This approach allowed us to segment the phases, e.g., pores in blue (Figure 7f) and kerogen in red (Figure 7g) from the matrix, which is rendered in grey as shown in Figure 7. Interactive thresholding is the binarization which transforms a grey level image into a binary image. This method is used when the relevant information in the grey level image corresponds to a specific grey level interval. This tool is a simple segmentation method and allows thresholds to be selected interactively.

The accuracy which with each of the matrix, kerogen and pore phases can be calculated essentially depends upon obtaining values of the threshold that separates on each of these phases. Consequently, the segmentation techniques should in principle be able to distinguish clearly between rock matrix, kerogen and pore space.

3. RESULTS

The microstructural properties obtained using Xμ-CT and FIB-SEM techniques can be described by a range of parameters, including porosity, permeability, pore volume, and pore size, pore aspect ratios, the surface area to volume ratio of pore and their distribution with scale; these results are presented in the following subsections.

3.1 3D Reconstructions of Gas Shale Volumes

The quantitative data presented in this sections were calculated from 3D reconstructions of both Xμ-CT and FIB-SEM image data using 3D image analysis software. An example of a reconstruction from Xμ-CT images is shown in Figure 8. The data set comprised of 1000 2D images, each comprising of square pixels with a side length of 0.94 μm.

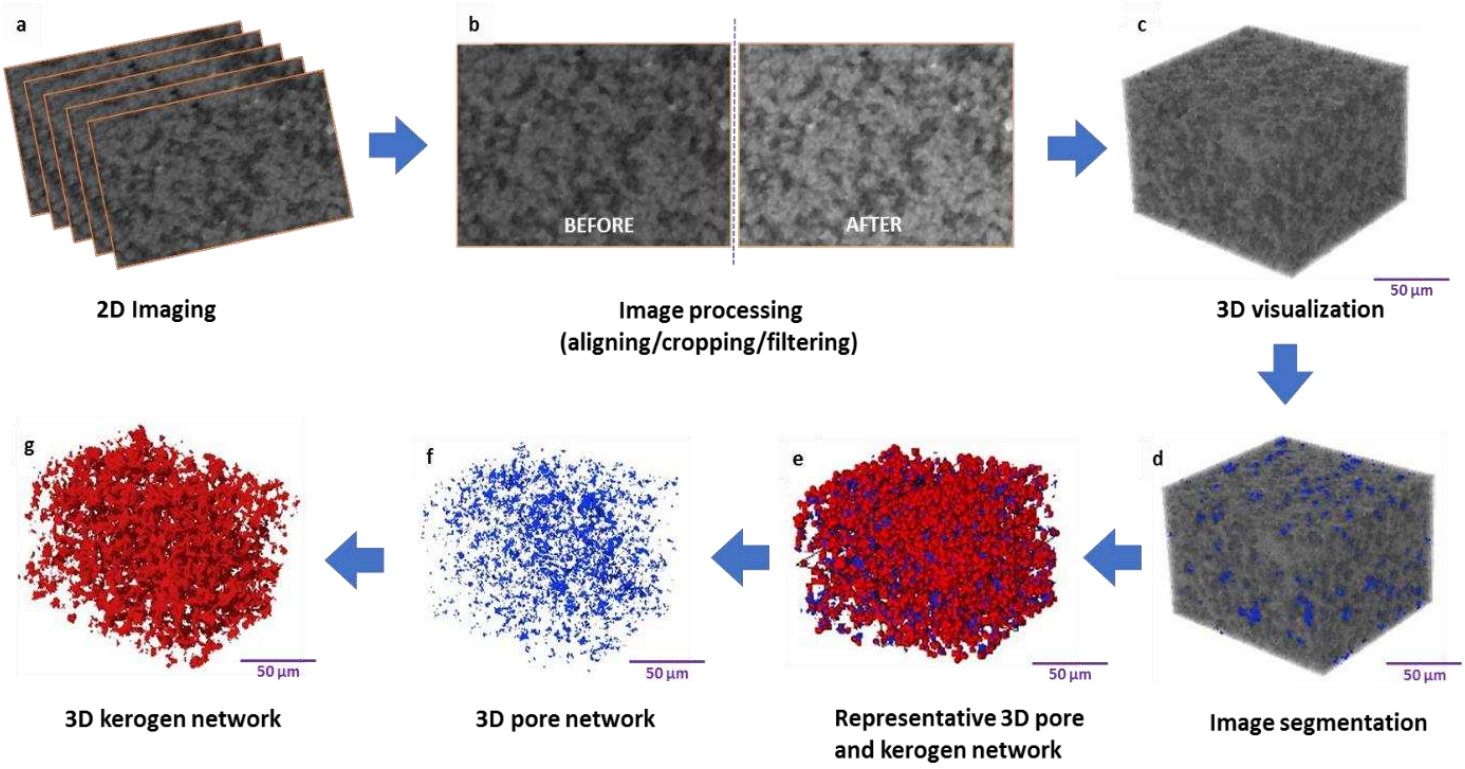

Figure 7. Schematic diagram of the procedure for analysing 3D datasets from Xμ-CT imaging techniques. Please see the text for details.

Figure 8a shows a raw 2D greyscale image of the sample. Using the greyscale of this raw data, threshold values can be set to define microstructural features of interest, particularly the kerogen and pores. Surfaces can then be generated around these regions within the thresholds. Figure 8b shows the 'non-local means' filtered 2-D greyscale image, this filter helps to remove the noise from the SEM and Xμ-CT images without damaging the images and keeping the same resolution of the pores. Figure 8c-d displays the 3D images of the kerogen and pores, respectively. A qualitative inspection of the connectivity of the pores and kerogen can then be performed, which is based on the thresholding procedure. For the estimated kerogen network observed in this sample, Figure 8c shows the kerogen in red and appears to be connected across the volume. The pore connectivity apparent from Figure 8d is less than that of the kerogen, with some interconnected pore spaces and some isolated pore spaces within the volume. These results suggest that the sample has a very small pore volume of only 6%, which may indicate that the pore system in the Bowland Shale has extremely low connectivity; this has also been reported by Ma et al. [10]. Thus the isolated pore space is unlikely to be important for gas transport at the different scales. However, the high connectivity observed for the kerogen (44.5%) becomes particularly important and provides potential pathways for gas transport throughout the samples [35, 36], but over a longer timescale. As a result of unconnected pores, the connectivity of kerogen suggests similar levels of connectivity to the published results of the Bowland Shale reservoirs from Ma et al. [10].

Figure 9a shows a 2D greyscale image of FIB-SEM shale of location A, while Figure 9b shows the non-local means filtered 2-D greyscale image. Figure 9c is a 3D representation of the kerogen present in the sample. This image shows the connectivity of the kerogen network across the 19×24×20 nm^3 sample volume. Figure 9d shows the pore spaces ranging in length from several nanometers to a few micrometers, that they vary in shape from spherical to elongated, and that they are connected, at least from a qualitative point of view. The volume contributions of kerogen and pores for the reconstructed raw gas shale volume from the FIB-SEM measurement were 34.8% and 10.0% respectively.

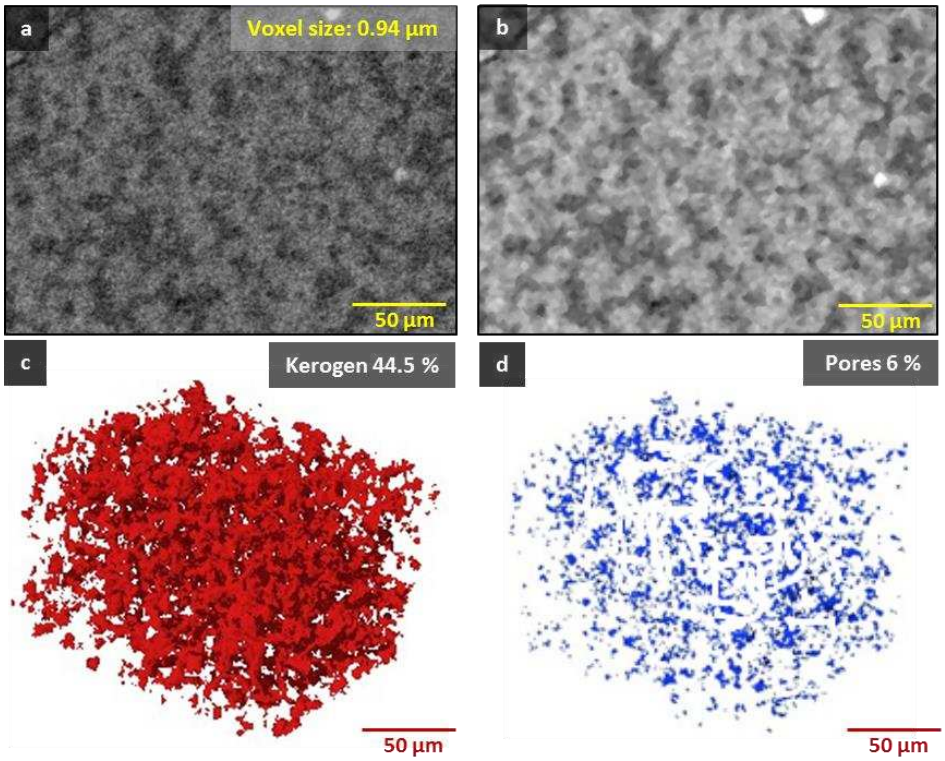

Figure 8. X-ray micro-tomography (Xµ-CT) for a shale rock sample acquired at a voxel size of 0.94 µm. (a) Raw 2D greyscale image, (b) Non-local means filtered 2D greyscale image. By setting thresholds on the greyscale of this 3D solid we can see (c) the kerogen shown in red, and (d) pores shown in blue.

3.2 Pore volume distribution

The 3D reconstructed volumes were used to estimate the relative frequency distribution of the volume of individual pores by both pore number and pore volume. Figure 10 shows histograms of pore-volume distribution as measured by FIB-SEM for the three different locations A, B, and C indicated in Figure 2, together with the pore-volume distribution as measured by Xµ-CT on the wider sample. The FIB-SEM and Xµ-CT data interrogate completely separate scales, with no overlap. Hence, the FIB-SEM data is shown in parts (a) and (c) of Figure 10, while the Xµ-CT data is shown in parts (b) and (d). The distribution of pore volume

can be displayed in terms of the percentage number of pores with a given pore volume, which is shown in parts (a) and (b) of the figure, or in terms of the percentage volume of pores represented by a given pore volume, which is shown in parts (c) and (d) of the figure. In the case of the pore number-based distribution, we have also included the log-log version of the data as insets, to show the well-developed power-law (fractal) behaviour of this measurement.

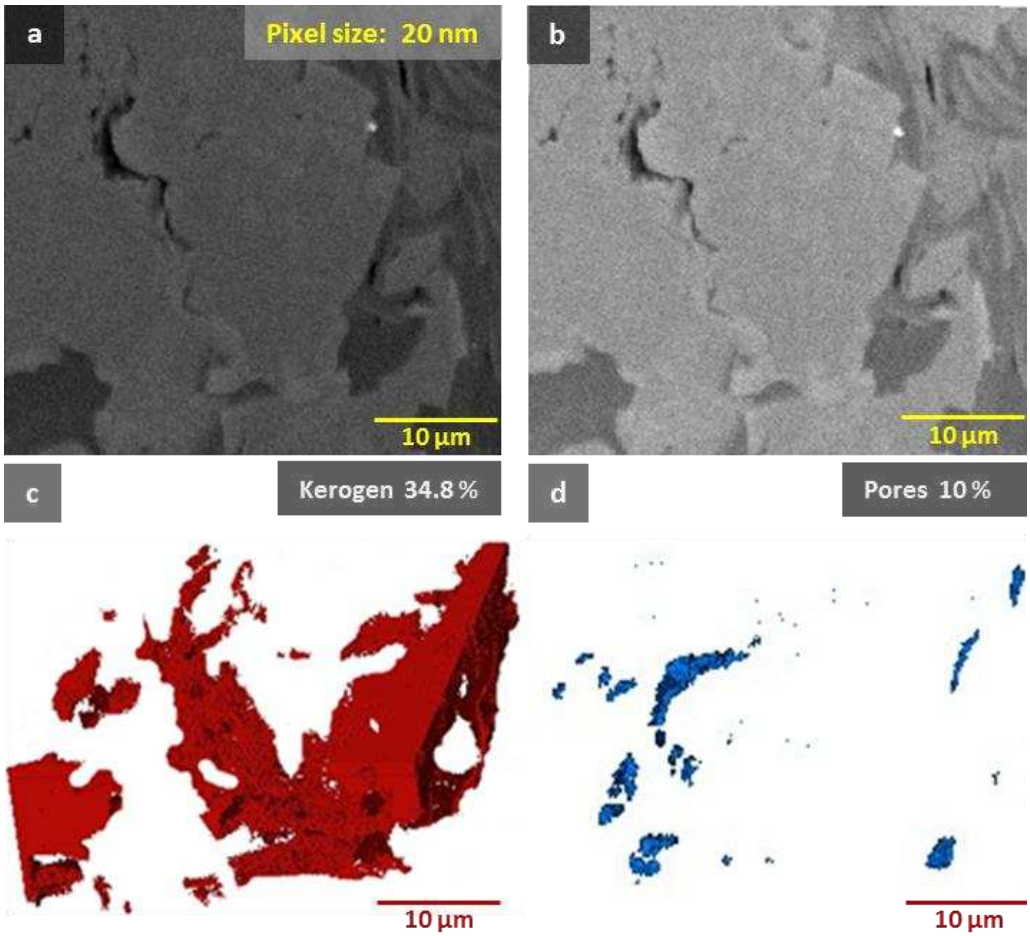

Figure 9. FIB-SEM assessment of the raw MD-2.7 km shale rock sample. (a) Raw 2D greyscale image, (b) non-local means filtered 2D greyscale image, (c) 3D representation of kerogen shown in red, and (d) 3D representation of pores shown in blue.

In terms of pore number, all of the FIB and Micro-CT samples show similar behaviour, which can be characterised as a power law distribution with a preponderance of the smallest pores and few larger pores. Power law fits, according to $y = px^q$, to these data are shown in Table 2 and show no well-defined generic pattern. These distributions are an indication that the pore number distributions have a fractal character, in common with many other natural phenomena, such as the number, length and aperture distributions of fractures in rocks.

Table 2. Power law fits to pore volume distributions.

Sample	Power-law fitting constant, p (-)	Power-law fitting exponent, q (-)	R^2
FIB-SEM-A	2.772×10^{-5}	-1.471	0.582
FIB-SEM-B	2.841×10^{-4}	-1.229	0.669
FIB-SEM-C	1.536×10^{-6}	-1.850	0.890
Micro-CT	40.365	-1.419	0.855

The differences in the curves and the associated fitting parameters is solely due to their difference scales of operation. In each case measurements increase as pore volume decreases until the resolution of the method is reached, with the minimum volume corresponding to the volume of the cuboidal voxel represented by that limiting resolution. Consequently, the relatively low resolution of the Xμ-CT technique (0.94 μm) cannot discriminate individual pores where the size of any of its dimensions is less than 0.94 μm, if they are present. By contrast, the FIB-SEM scan can recognise pores with a minimum extent of 0.02 μm for FIB-SEM-A and 0.05 μm for the other two FIB-SEM samples. If the pores are equant, the minimum pore volumes would be about 1 μm^3 and 0.00001 μm^3 for the Micro-CT and FIB-SEM data, respectively. The fact that the data finishes at higher values than these ultimate limits is an indication that some very fine pores are unmeasurable because one of their dimensions is lower than the resolution even when other dimensions are above it.

In principle the FIB-SEM method can recognise pores as large as $20\times20\times1$ μm^3, but the power law distribution shows that the chances of the volume being measured by the FIB-SEM method containing one of these larger pores is very small, and if it did so the volume would be unrepresentative of the wider sample. Hence Figure 10a shows negligible pore volumes larger than 0.02 μm^3 even though the Xμ-CT measurements (Figure 10b) confirm they exist.

The apparent lack of data between 0.01 μm^3 and 0.9 μm^3 shown in Figure 10 does not indicate that no pores exist with these volumes, but that such pores are not recognised by either of the two techniques we have used. A third technique would be needed to fully investigate the sample. Nano-scale CT (Xn-CT) measurements (with a voxel size of ca. $0.05\times0.05\times0.05$ μm^3) allow such measurements to be made and will be reported in a further paper.

Parts (c) and (d) of Figure 10 show the same data but plotting the fraction of the total pore volume represented by pores of a given volume. Comparing this data with the data for pore number shows clearly that while pores with small volumes dominate in number, they do not dominate in volume. Indeed, for both FIB-SEM and Xμ-CT data, the larger less numerous pores contribute equally significantly to the overall pore volume.

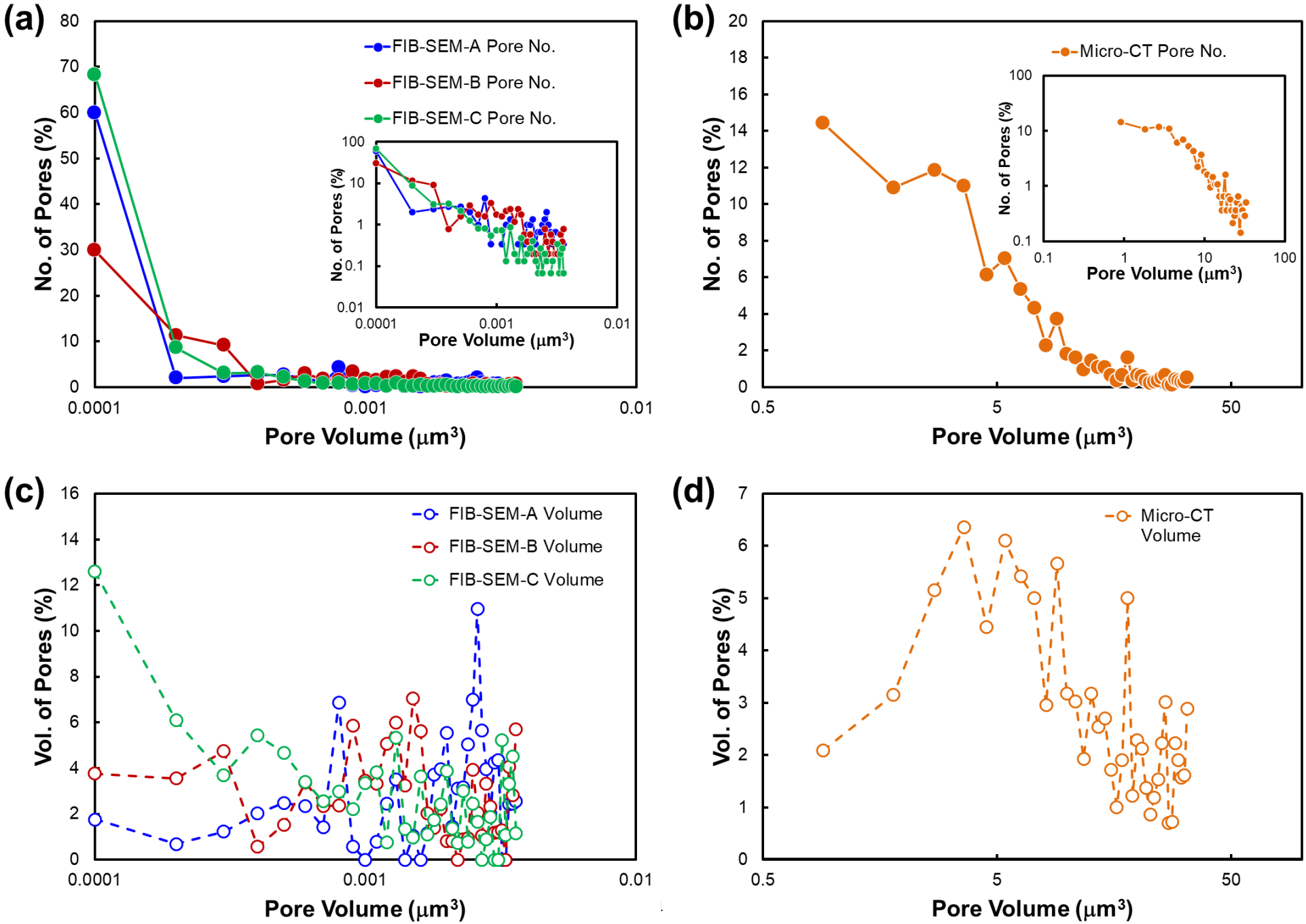
(a)
FIB-SEM-A Pore No.
FIB-SEM-B Pore No.
FIB-SEM-C Pore No.
No. of Pores (%)
Pore Volume (μm³)
(b)
Micro-CT Pore No.
No. of Pores (%)
Pore Volume (μm³)
(c)
FIB-SEM-A Volume
FIB-SEM-B Volume
FIB-SEM-C Volume
Vol. of Pores (%)
Pore Volume (μm³)
(d)
Micro-CT Volume
Vol. of Pores (%)
Pore Volume (μm³)

Figure 10. The distribution of pore volume on the basis of numbers of pores representing a given pore volume, for (a) FIB-SEM, and (b) Xμ-CT for sample MD-2.7 km of a gas shale rock from the Bowland formation. Insets show the same data on a log-log scale. The distribution of pore volume on the basis of the volume of pores representing a given pore volume, for (c) FIB-SEM, and (d) Xμ-CT.

Each of the two techniques provides data over a specific range of scales and represent that data as a relative frequency. That is to say, each set of measurements assumes in the calculation of the relative frequency that there is no pore volume existing at scales lower than its resolution or higher than its field of view. This is clearly not true. The result is that the data in Figure 10 for the three locations measured by FIB-SEM can be compared directly, the data for the two techniques (any of the FIB-SEM curves and the Xμ-CT curve) cannot be compared as both are subject to an unknown scaling. This problem could be obviated by an overlap in measurement ranges, but there is insufficient overlap to do so in this case. The implementation of a third technique whose imaged data spanned both of the techniques would supply a solution, and help scale each of the curves such that they represented the same relative frequency. Such a technique exists in nano-CT imaging, and it is recommended that this approach is used in future.

3.3 Pore aspect ratio distributions

The three-dimensional shape of any pore can be approximated by the use of pore aspect ratios. The most common approach is to assume that any pore can be represented by an ellipsoid such as that shown in Figure 11. Pore aspect ratios are the ratios of the radii in any two of the x, y, and z directions, which are labelled a, b and c in the figure. While a total of six pore aspect ratios can be defined, three are simply inverse of the other three, and of the basic three, only two are required to fully define the shape of the ellipsoid. We choose to use two pore aspect ratios. The first is given by $\gamma_1 = c/b$ (Figure 12a,b), where b is the maximum dimension of the pore, and c is its width, being defined as the minimum dimension of the pore. The second aspect ratio is given by $\gamma_2 = a/c$ (Figure 12c,d), where a is the radial extent of the pore mutually perpendicular to both b and c. The pore aspect ratios are measures of the shape of the pore. If the pore is penny–shaped (oblate), $a \approx b >> c$, with γ_1 <<1 and γ_2 >>1. If the pore is pin–shaped (prolate), $a \approx c << b$, with γ_1 <<1 and $\gamma_2 \approx 1$. The value of both pore aspect ratios is important because pores which are long and thin ($\gamma_1 \ll 1$) or have a significant sideways extent ($\gamma_2 \neq 1$) have a greater potential for connecting up with other pores, contributing to raising the chances that the pore structure forms an interconnected network which will support gas flow. Most grain boundary pores, parting surfaces in shales and fractures are better modelled by oblate spheroids with $\gamma_1 \ll 1$.

It should be noted that in the calculation of the pore aspect ratios, the local Cartesian directions are rotated to ensure that they are aligned with the largest and smallest dimensions of the pore. Consequently, the pore aspect ratios are scalar quantities

describing the mean geometry of pore structures and contain no information about any alignments or anisotropy of pore structure within the rock.

In this work both γ_1 and γ_2 were calculated for each pore in the data set from both FIB-SEM and Xμ-CT measurements.

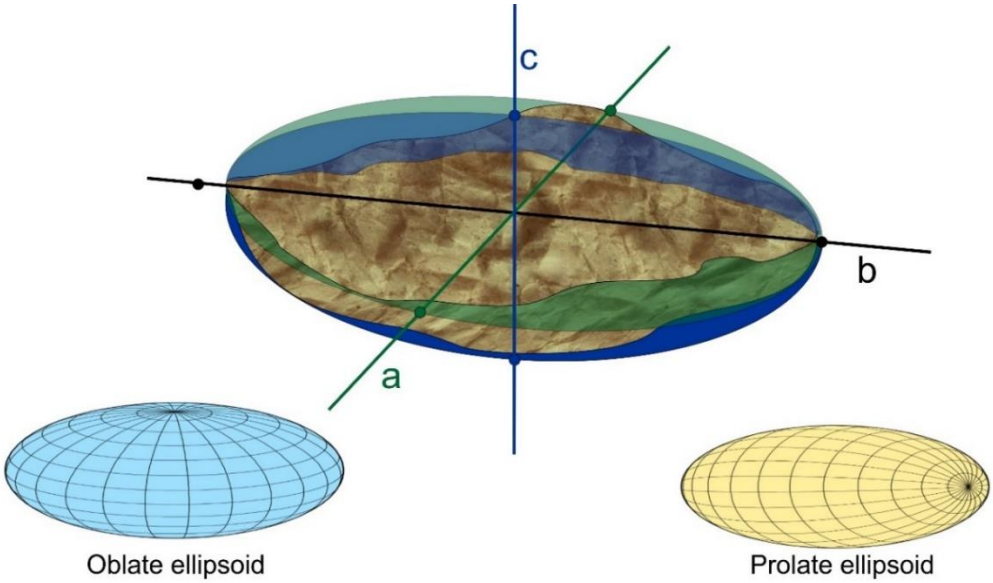

Figure 11. Diagram illustration of an irregular pore (textured) with a fitted ellipsoid with major radii a, b and c. The subsidiary diagrams show the form of an oblate ellipsoid and prolate ellipsoid.

Figure 12 shows a plot of the distribution of the number and volume of pores as a function of the pore aspect ratio, as estimated by both FIB-SEM and Xμ-CT techniques. Parts (a) and (b) show the γ_1 aspect ratio distribution in terms of number and volume, respectively. In both of these graphs a value approaching unity indicates a more equant pore. The pore number distribution (Figure 12a) shows that there are negligible equant pores, but significant numbers of pores occur in the range $0.8>\gamma_1>0.1$, which is equivalent to saying that the pores in the shale have a long axis between 1.25 and 10 times longer than their smallest axis (width or aperture). It is interesting to note that the range of pore shapes indicated by all four measurements are similar for the FIB-SEM-A and Xμ-CT data despite these two techniques measuring different populations of pores at very different scales. There seems to be a propensity of pores with a value of about γ_1=0.2 (length equal to five times the aperture) in the FIB-SEM-A and Xμ-CT data, and a preference for about γ_1=0.47 for the other 2 FIB-SEM measurements.

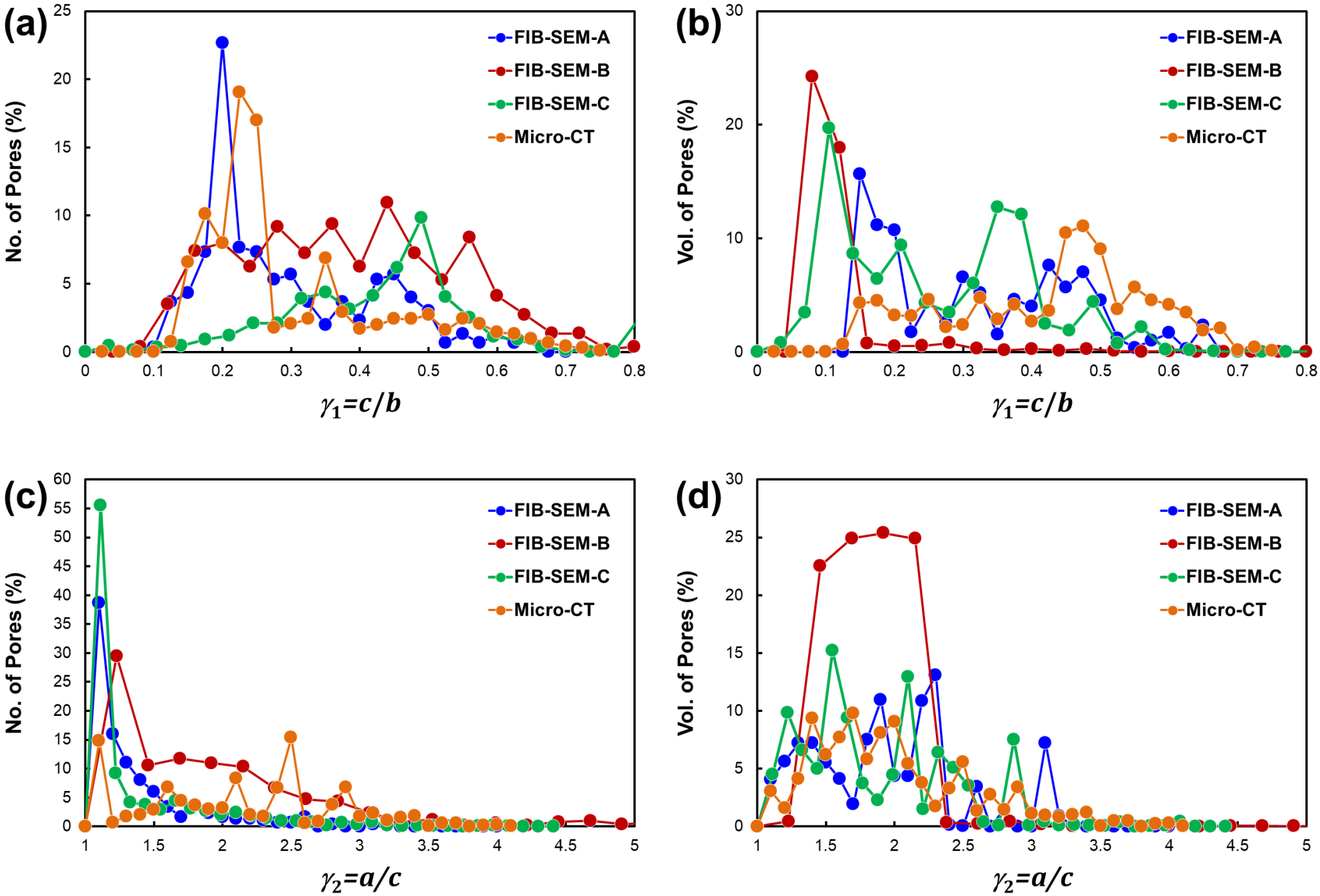
(a)
No. of Pores (%)
FIB-SEM-A
FIB-SEM-B
FIB-SEM-C
Micro-CT
$\gamma_1=c/b$
(b)
Vol. of Pores (%)
FIB-SEM-A
FIB-SEM-B
FIB-SEM-C
Micro-CT
$\gamma_1=c/b$
(c)
No. of Pores (%)
FIB-SEM-A
FIB-SEM-B
FIB-SEM-C
Micro-CT
$\gamma_2=a/c$
(d)
Vol. of Pores (%)
FIB-SEM-A
FIB-SEM-B
FIB-SEM-C
Micro-CT
$\gamma_2=a/c$

Figure 12. The pore-aspect ratio distribution, (a) pore-aspect ratio distributed as a function of the number of pores obtained from γ_1 (oblate) values, (b) pore-aspect ratio distributed estimated from γ_1 values as a function of the total volume of pores, (c) pore-aspect ratio distributed as a function of the number of pores as calculated from γ_2 (prolate) values, (d) pore-aspect ratio distributed estimated from γ_2 as a function of the total volume of pores, estimated as by FIB-SEM and Xμ-CT using the sample MD-2.7 km of gas shale from the Bowland formation.

The number distribution, however, does not necessarily represent the relative importance of pores at each scale in a balanced way. It cannot, for example, be used to infer which pores provide better gas storage capacity because it treats pores of all sizes equally when those which are larger clearly will contribute more to gas storage. Consequently, we have also plotted the volume of pores against their pore aspect ratios. Figure 12b shows a plot of the percentage of the overall pore volume represented by pores with different γ_1 values. When viewed this way, significant volumes of pores occur in the range $0.7>\gamma_1>0.05$, which is equivalent to saying that the pores in the shale have a long axis between about 1. 5 and 20 times longer than their smallest axis (width or aperture). All of the FIB-SEM data is in agreement that the majority of the pore volume is in the form of pores with $\gamma_1>0.25$ (4 times longer than wide), while the larger scale Xμ-CT data has a maximum at about $\gamma_1=0.475\pm0.035$, while FIB-SEM-C has a subsidiary peak at about $\gamma_1=0.37\pm0.04$.

Consequently, the data presented in this work indicates strongly that the pores in this shale are at least twice as long as wide and up to 20 times in many cases, with the longer, thinner pores occurring at the smaller scales, measured by FIB-SEM, and the more equant pores occurring at the larger scales and measured by Xμ-CT.

Parts (c) and (d) of Figure 12 show the distribution of γ_2 values with respect to percentage pore number and percentage pore volume, respectively. In these plots a value of γ_2 approaching unity indicates that the breadth of the pore approaches that of its width. Since we know its length is larger than these two measures, a value of unity indicates a prolate pore. The pore number distribution shown in Figure 12c suggests that the greatest number of pores in the samples, whether measured by FIB-SEM at all of the locations or by Xμ-CT is close to unity, and that consequently the pores in the shale are overwhelmingly prolate, at least from the point of view of pore number.

Figure 12d shows the same data in terms of percentage pore volume. This figure shows that most of the pore volume is present in pores which have $1.5<\gamma_2<3$, indicating that pores which represent significant volume are slightly flattened (penny shaped) but never more

than three times as broad as they are wide, while those truly prolate pores that represent the peaks in Figure 12c account for less than 5% of the pore volume overall.

Once again, it is worth noting the similarity in the γ_2 behaviour between the FIB-SEM data and the Xμ-CT data even though the data is for four different populations of pores at two very different scales.

Different shales will exhibit different aspect ratios, implying differences in pore connectivity and consequently in their gas permeabilities. Shales which have lower values of γ_1 and higher values of γ_2 should offer the greatest permeability. Our results suggest that while there is no clear difference in the pore aspect ratio distributions measured by FIB-SEM and by Xμ-CT, the large number of pores with $\gamma_1 << 1$ and $\gamma_2 >> 1$ existing at nanoscale and imaged using FIB-SEM may represent a pervasive nanoscale pore network that cannot be recognised by Xμ-CT imaging.

3.4 Pore surface area to volume ratio

The pore surface area to volume ratio (ξ) is another potential useful indicator of pore shape. A spherical pore represents the most efficient use of surface area to contain a given volume, while higher values of surface area to volume ratio indicate the presence of a larger surface area per unit volume of pore space, which occurs as the pore shape changes from that of a perfect sphere, particularly if the pore becomes oblate.

The shape of the pores can be significant in shale gas reservoirs in a number of ways. For example, pores that are more spherical are much less likely to collapse under externally applied pressure than crack-like or linear pores, which tend to close easily when subjected to only a small normal stress [4]. Consequently, sub-horizontal crack-like pores observed in samples at surface pressures are very unlikely to remain open at reservoir depths. However, long, thin pores are more likely to interact with other pores and cracks, making them much more effective at increasing pore connectivity and leading to higher permeability [37]. Perhaps most importantly, large surface areas facilitate the diffusion of gas initially trapped in the matrix of the rock and in the kerogen into the pore spaces within the shale [37]. This is an essential stage before hydraulic fracturing can open up access to these small pore spaces. A high surface area thus ensures that the diffusion procedure is more efficient, not only ensuring a good initial charge of gas in the micro-pores of the shale, but also allowing those pores to be recharged quickly once initial production has removed the initially accumulated gas.

High values of surface area to volume ratio might indicate a flatter pore shape. Unfortunately, the surface area to volume ratio has dimensions of per-length which means that smaller pores also generate high surface area to volume ratios. Consequently, we have defined a new parameter which incorporates the effect of surface area to volume, but normalises it in such a way that the parameter is unitless, and hence will be invariant to pore size.

The concept of surface area to volume ratio is best understood by assuming all the pores in the rock can be described by an ellipsoid of either oblate or prolate types, as defined earlier in Figure 11. In this work we define the long axis of an ellipsoid as b, the smallest axis as c and the intermediate axis as a. Oblate spheroids have semi-axis sizes according to $b \approx a > c$, i.e. spheres squashed in the *c*-direction, and approximate to penny-shaped cracks or pores. By contrast, prolate spheroids have semi-axis sizes conforming to $b > a \approx c$, i.e., spheres stretched in the *a*-direction, and approximate to needles. The volume of both types of spheroid can be calculated using the formula:

$$V = \frac{4}{3}\pi abc. \quad \textbf{(1)}$$

The surface areas of the two types of spheroid differ and can be expressed fully by using elliptic integrals which are outside the scope of this paper. However, the value of the surface area to volume ratio for a sphere is $\xi_{sphere} = \frac{3}{a}$, and that value becomes larger if the sphere decreases in size. The surface area to volume ratio also becomes larger as the ellipsoid becomes more oblate.

In order to remove the functional dependence of surface area to volume ratio on the size of the pores, we have decided to institute a parameter which we call the scale invariant surface area to volume ratio, and give it the symbol σ. We define the scale invariant surface area to volume ratio as

$$\sigma = a\xi, \quad \textbf{(2)}$$

which is the conventional surface area to volume ratio multiplied by the intermediate semi-axis of the ellipsoidal pore, in this case a. The value of σ varies from 3, which represents a sphere to infinity as the ellipsoidal pore becomes more oblate or prolate.

Figure 13 shows the distributions of the percentage number and percentage volume of pores as a function of the scale-invariant surface area to volume ratio, σ, as measured by both Xμ-CT and FIB-SEM techniques. Considering the pore number distribution (Figure 13a), the values obtained from all three FIB-SEM measurements and the Xμ-CT measurement are in agreement. No values are less than 3, but there are peals in all of the distributions close to 3. This agrees well with the pore volume and aspect ratio data, and is expected to describe the preponderance of very small pores that are accounted for by a single voxel in each of the measuring techniques. It should be noted that the value of σ for a cubic voxel is 6, but decreases as it becomes a cuboid shortened in one direction. This is consistent with the values of the peaks in Figure 13a. However, this figure also shows measureable numbers of pores with values of σ extending to about σ=18, indicating the presence of pores which have a significantly enhanced surface area for their volume.

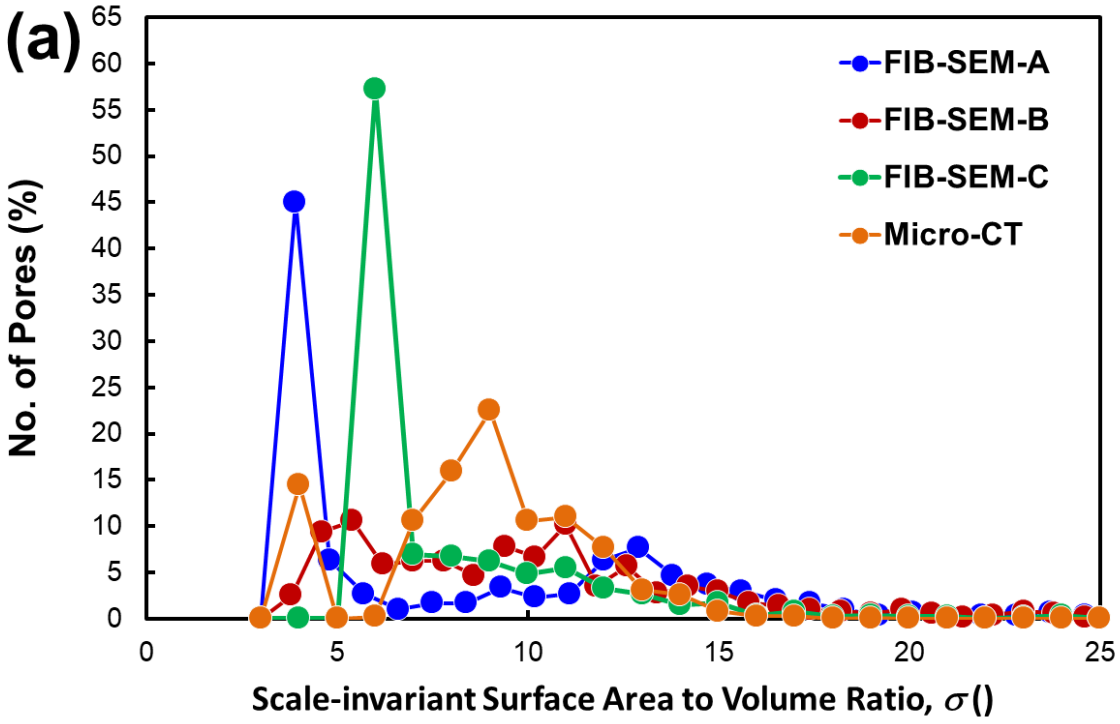

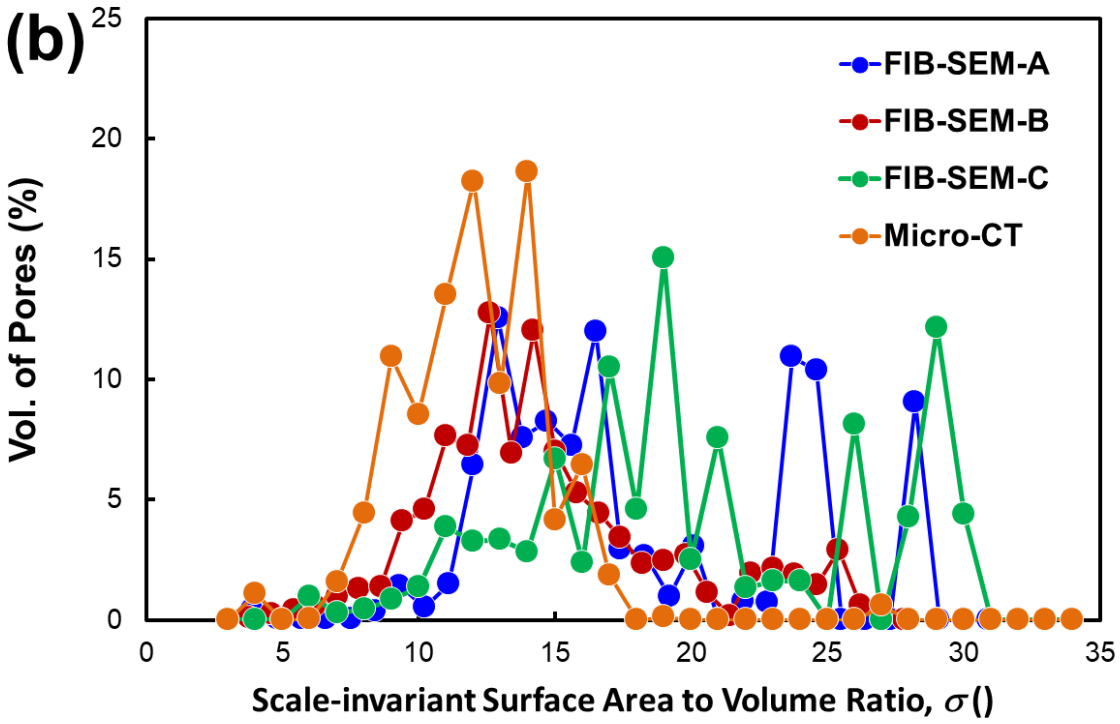

Figure 13. Showing the scale-invariant pore surface area to volume distribution, σ, calculated from FIB-SEM and Xμ-CT measurements of sample MD-2.7 km; (a) distribution with respect to the percentage of the total numbers of pores, (b) distribution with respect to the percentage of the total volume of the pores.

When the percentage volume contribution of each value of the scale-invariant surface area to volume ratio is considered (Figure 13b), it is clear that all three of the FIB-SEM measurements and the Xμ-CT measurement are in agreement that the pores which contribute significantly to the overall pore volume have scale-invariant surface area to volume ratios which are large, falling in the range $10<\sigma<30$.

Consequently, it may be said that there are pores of significant pore volume in the shale sample which have a large surface area for gas desorption.

3.5 Permeability

The permeability of a rock can be estimated by using the standard pore surface area to volume ratio, ξ. The mean effective pore radius can be calculated following the approach used by Johnson et al. [38], where they defined an effective pore diameter $\xi=2V_p/S_p$, where V_p is the pore volume and S_p is pore surface area of pores [34]. Thus, the parameter Λ is defined by $\Lambda=2/\xi$. The Λ-value is a measure of the aperture for fluid flow which controls the permeability in the sample according to the relationship $k = \Lambda^2/8F$, where $F = \phi^{-m}$ is the formation factor of the rock [39]. In this equation the value of Λ describes the size of opening pores between the grains which allow the passage of fluid, while the formation volume factor contains information about how inter-connected those pathways are [37-40]. The formation volume factor was not measured directly in this work, but was estimated using the measured porosity for the sample and an assumed value of the cementation exponent m=3. This value was chosen since the cementation exponent m for shales is known to vary between about 2.34 and 4.17 [41].

Using the method described previously, the calculated permeabilities for the MD-2.7 sample were found to be 13.85±3.45 nD, 4.16±1.04 nD, 150±37.5 nD and 2.98±0.745 nD for FIB-SEM locations A, B, C and from Xμ-CT, respectively (Table 1). These values are broadly in agreement with recent up-scaled permeability determinations for the Barnett shale [49]. It is worth observing that location C does have a larger permeability and porosity than locations A and B as well as at a larger scale from Xμ-CT measurements. We ascribe the observed difference for location C as due to this location containing a large crack, which can be seen in Figure 6c.

The dimensions of the interconnected pores have an important role in our estimation of permeability, and hence an appropriate theoretical method for the effective pore radius or pore throat size is required. In order to validate the previous permeability calculations, Avizo® software has been used on SEM images of samples to measure the equivalent circular diameter of a crack.

Figure 14 shows an SEM image for location C with a large crack. The crack has a length of about 10.4±0.02 μm, and is approximately 0.2±0.02 μm wide. The equivalent diameter of the crack has been calculated with following equation Jennings et al. [48]:

$$d_e = 1.3(ab)^{0.625} / (a+b)^{0.25} \quad \textbf{(8)}$$

Where; d_e is equivalent diameter (µm), a is the length of crack (µm) and b is the width of the crack (µm). For the crack shown in Figure 14 the equivalent diameter from Equation 8 is about 1.12±0.06 µm. If we assume that this value can be used to represent the characteristic pore size in the Johnson et al. equation given above [38], with m=3, the permeability is predicted to be 131.54±13.15 nD, which is remarkably consistent with the value obtained from the value of ξ calculated earlier for this location (150±37.5 nD).

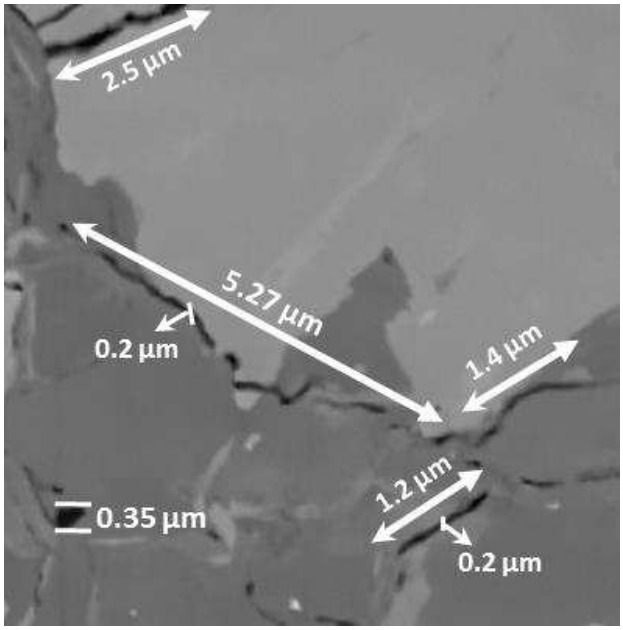

Figure 14. SEM image of location C with the dimensions of cracks. Uncertainties ±0.02 µm.

Table 1 towards the beginning of this paper shows a summary of the most significant data including porosity, image size and voxel size for the sample MD-2.7 km obtained using both FIB-SEM and Xµ-CT techniques. The porosities of intermediate-rich samples for locations A, B and C (i.e., pore volume/ total volume of rock) were found to be 0.10%, 0.52%, 0.94%, respectively. Location C had a significantly higher porosity than the other two; possibly due to the cracks which can be seen in Figure 6.

While it is pleasing that the combination of FIB-SEM, Xµ-CT imaging and 3D image analysis has produced a reasonable value of porosity on the basis of this sample, it is recognized that the approach needs to be validated using independent porosity measurements such as nano-CT on multiple samples. Such measurements are envisaged as part of the future work programme.

4. DISCUSSION

In this study, we have characterised Bowland Shale using a single sample at multiple scales with multiple techniques. Although a few studies on Bowland Shale reservoirs have previously considered a few scales of observations [10], none has been as comprehensive, imaging a single sample volume using Xμ-CT measurements, then making higher resolution FIB-SEM within the original sample volume but at specific multiple locations, each with a smaller field of view.

The results of the imaging in our study show that FIB-SEM analysis indicates that most pores in the scale range measured by that technique have a volume in the range 10^{-5} μm^3 to 0.0036 μm^3, while from Xμ-CT analysis measured pore volumes are from is 0.9 μm^3 to 31.5 μm^3 (Figure 10). These data represent the measurement of two different populations of pores existing at different scales and measured with the different techniques. The lack of overlap in the scale ranges of the FIB-SEM and Xμ-CT data means that no reasonable combination of the data into a single dataset with a wider scale range can be carried out, and hence we have plotted this data separately. Additional data is required from another source if the FIB-SEM and Xμ-CT datasets are to be integrated. The Nano-CT 3D imaging method may fill this gap, and is currently being studied.

These data are also skewed by the preponderance of small pores at the limits of the resolution of each technique that appear as a large number of single voxel pores. Plotting the distributions to show the percentage contributions to the pore volume shows that the smaller number of pores with larger pore volumes account for more of the overall pore volume of the rock.

Clearly, the two different techniques are measuring different populations of pores which occur at different scales; one at the micrometre scale and the other at the nanometre scale. Consequently, we can say that the use of Xμ-CT data to characterise a shale will fail to take account of that population of pores which is smaller than the resolution of the Xμ-CT technique. Such a failure might be extremely significant if the nanoscale pores prove to control the connectivity of the pore network, which is likely to be the case since pores imaged by Xμ-CT seem very isolated (Figure 8), which has also been observed in the work of Ma et al. [10]. The permeability of shales, though small, is measureable, falling in the range 10 – 250 nD. Equally, sole use of FIB-SEM measurements will fail to detect pores in the microscale range, missing potential significant contributions to the overall porosity, and hence the available storage capacity of the rock

The smallest pore visible obtained for the sample, from FIB-SEM has a volume of 6.532×10^{-6} μm^3 in Location A, which corresponds to a pore diameter of 25.5 nm if a spherical pore is assumed, or 18.7 nm if a cubic voxel is assumed. The smallest pore imaged by this technique is, therefore, not necessarily the smallest pore in the rock because the voxel size for our implementation of this technique is 19x24x20 nm^3, as discussed in the methodology section. The largest volume in this location was about 0.027 μm^3, equating to a pore diameter of about 411 nm, which may be similarly constrained by the size of the imaged volume (20x20x1 μm^3).

The data given in Figure 12 has shown that pores which contribute significantly to the pore volume of the rock have aspect ratios indicating that they are broader than their smallest dimension by up to five times, but critically that they may be up to 10 or 20 times their aperture in length, for both the larger population of pores imaged by Xμ-CT and the smaller scale pores imaged by FIB-SEM. These high aspect ratio pores are more likely to interlink and give these shales a larger permeability, which is consistent with the permeability values we have calculated (Table 1).

Data presented in Figure 13 shows that pores which contribute significantly to the pore volume of the rock also have significantly raised values of scale-invariant surface area to volume ratio. Pores with large surface area to volume ratios allow for a much more efficient desorption of gas from the matrix and kerogen into the pores and hence contribute to efficient gas production.

Consequently, we can say that the shale studied in this work combines three important interlinked characteristics, in that (i) the pores which compose the significant proportion of the pore volume (ii) have shapes that enhance their interconnectivity and hence permeability, while (iii) also enhancing gas desorption from the matrix and kerogen into the pore space.

The shape of pores is also significant in defining the geomechanical properties of the rock. Shales have an inclination to plastic behaviours and any tendency towards weakness is likely to result in the closure of fractures and pores. While it is generally accepted that high aspect ratio, high surface area to volume penny-shaped pores and cracks are much more prone to closure than those with low aspect ratios and low surface areas to volume [6, 39, 40], many other factors, such as the *in situ* stress, rock strength, pore pressure, also effect the geomechanics of a pore and fracture network. It is not, therefore possible to definitively associate high aspect ratio, high surface area to volume pore spaces with the volume and duration of gas production. Consequently, on balance, high aspect ratios and large surface areas are beneficial for shale in term of gas production.

It has been indicated in the literature that not only pore volume and size, but also pore and fracture surfaces are fractal [43, 44, 45]. If so, such fractal cracks or pores can in principle have a surface area to volume ratio that is infinite. Therefore, it should be considered that some samples might have much higher surface areas due to the roughness of their surfaces, which do not substantially increase the pore volume but provide much larger pore surface areas. Approaches that take into consideration the fractal distribution of properties such as porosity and grain size are now being implemented in new reservoir modelling approaches and used to create fractal permeability models for shale gas flow (e.g., [28, 46, 47]).

The main limitation of FIB-SEM and Xμ-CT imaging for all measured parameters is that they have sharply defined scale ranges which do not overlap. Consequently, pores which are

either lower or higher than the resolution or field of view will not be taken into consideration. It is possible to plot the data on a combined scale, as we have done in Figure 10, but there is no method for scaling the FIB-SEM and Xμ-CT distributions such that they represent the same relative frequency. Such an integration would have been possible if the ranges for each of the measurements overlapped, but unfortunately they do not. This is a particular problem for generating a pore volume distribution across a wide range of scales, or in the estimation of permeability, where the relative heights of peaks in the relative frequency measurement would allow the dominant pore volume or volumes to be ascertained. One solution would be to find a 3D imaging method that operates over a range of scales overlapping with both the FIB-SEM and Xμ-CT imaging techniques. Such a methodology exists in nano-scale CT imaging. We have carried out such imaging and the results will be published in a further paper.

5. CONCLUSIONS

In this paper, we have imaged samples of shale reservoir rock by using FIB-SEM and Xμ-CT technology in order to investigate the microstructure of gas shale at a wide range of scales (from 20 nm to 0.5 mm). The results show a complex microstructure that varies significantly between different regions in the sample and as a function of scale.

Samples were primarily composed of different amounts of pores and kerogen. The porosity varied from 0.06% to 0.94% and the kerogen fraction varied from 34.8% to 44.5%. Overall, the pore volume observed by SEM for the three locations spanned over a range of 10^{-5} μm^3 to about 31.5 μm^3, while the corresponding range for Xμ-CT analysis was between 1 μm^3 to 1×10^3 μm^3. Computer-generated 3D renderings of shale volumes were reconstructed from serial sectioning and imaging-enabled qualitative analysis of kerogen and pore connectivity across the volumes. Quantitative analysis of these renderings allowed for estimates of percentage kerogen and porosity by volume for the shale samples. Estimated distributions of pore aspect ratio and surface area to volume ratio showed that an important feature of a shale gas rock is its connectedness which regulates permeability. Our results suggest that pores in the scale range accessed by the Xμ-CT technique are apparently isolated, but the smaller pores imaged using FIB-SEM form a connected pore network which engages with the larger pores measured by Xμ-CT. Hence, the larger pores control the porosity and storage capacity of the rock, while the smaller pores control the ability of fluid to flow through the rock. This observation is consistent with the work of Ma et al. [10].

The shape of the pores can be significant in shale gas reservoirs because pore shape regulates the rate of gas desorption and ultimately controls the recharging of gas in pores and fractures. The scale-invariant pore surface area to volume ratio (σ) for pores which contribute significantly to the overall pore volume has been found to range from 10 to 30. The pore shape also controls the mechanical properties of the rock and the likelihood that pores will interlink to form a pervasive pore network for fluid flow.

6. ACKNOWLEDGMENTS

The authors would like to thank Cuadrilla Resources Ltd. for providing the samples and the Leeds University Electron Microscopy and Spectroscopy Centre (LEMAS) for technical support (Stuart Micklethwaite and John Harrington), with special thanks to Mr John Wyn Williams of Leeds University School of Earth and Environment for sample preparation.

REFERENCES

1. Shar, A. M., Mahesar, A. A. & Memon, K. R. 2017. Could shale gas meet energy deficit: its current status and future prospects. Journal of Petroleum Exploration and Production Technology, 8, 957-967.
2. EIA. 2020. Annual Energy Outlook 2020 with projections to 2050. Retrieved from January 2020, https://www.eia.gov/outlooks/aeo/pdf/aeo2020.pdf
3. EIA. 2019. U.S. Crude Oil and Natural Gas. U.S. Energy Information Administration. Retrieved December 2019, from https://www.eia.gov/naturalgas/crudeoilreserves/pdf/usreserves.pdf
4. Curtis, M.E., Ambrose, R.J., Sondergeld, C.H. and Rai, C.S. 2011. Investigation of the relationship between organic porosity and thermal maturity in the Marcellus Shale. Paper presented at the North American Unconventional Gas Conference and Exhibition, SPE-144370-MS.
5. Ambrose, R.J., Hartman, R.C., Diaz-Campos, M., Akkutlu, I.Y. and Sondergeld, C.H. 2010. New pore-scale considerations for shale gas-in-place calculations. SPE-131772, paper presented at the Unconventional Gas Conference, SPE, Pittsburgh, PA, February 23-25.
6. Curtis, M.E., Ambrose, R.J., Sondergeld, C.H. and Rai, C.S. 2010. Structural characterization of gas shales on the micro- and nano-scales. Paper SPE-137693-MS presented at the SPE Canadian Unconventional Resources and International Petroleum Conference, Calgary, Canada.
7. Vandenbroucke, M., Largeau, C. 2007. Kerogen origin, evolution and structure. Organic Geochemistry, 38, 719 – 833.
8. Amann-Hildenbrand, A., Ghanizadeh, A., Krooss, B.M. 2012. Transport properties of unconventional gas systems. Marine and Petroleum Geology, 31, 90-99.
9. Clarkson, C.R., Freeman, M., Heb, L., Agamalian, M., Melnichenko, Y.B., Mastalerz, M., Bustin, R.M., Radlinski, A.P., Blach, T.P. 2012. Characterization of tight gas reservoir pore structure using USANS/SANS and gas adsorption analysis. Fuel, 95, 371-385.
10. Ma, L., Taylor, K. G., Lee, P. D., Dobson, K. J., Dowey, P. J and Courtois, L. 2016. Novel 3D centimetre-to nano-scale quantification of an organic-rich mudstone: The Carboniferous Bowland Shale, Northern England. Marine and Petroleum Geology, 72, 193-205.
11. Guise, P., Grattoni, C. A., Allshorn, S. L., Fisher, Q. J and Schiffer, A. 2018. Stress Sensitivity of Mercury-Injection Measurements. Petrophysics, 59, 25-34.
12. Yuan, Y. & Rezaee, R. 2019. Comparative Porosity and Pore Structure Assessment in Shales: Measurement Techniques, Influencing Factors and Implications for Reservoir Characterization. Energies, 12.

13. Sakellariou, A., Sawkins, T.J., Senden, T.J., Arns, C.H., Limaye, A., Sheppard, A.P., Sok, R.M., Knackstedt, M.A., Pinczewski, W.V., Berge, L.I. and Øren, P.E. 2003. Micro-CT facility for imaging reservoir rocks at pore scales. SEG Annual Meeting, Dallas, Texas, October 26-31.
14. Long, H., Swennen, R., Foubert, A., Dierick, M. and Jacobs, P., 2009. 3-D quantification of mineral components and porosity distribution in Westphalian C sandstone by microfocus X-ray computed tomography. Sedimentary Geology, 220, 116-125.
15. Goral, J., Miskovic, I., Gelb, J. and Andrew, M. 2015. Correlative XRM and FIB-SEM for (non) organic pore network modeling in Woodford shale rock matrix. In International Petroleum Technology Conference. International Petroleum Technology Conference
16. Hemes, S., Desbois, G., Urai, J. L., Schröppel, B. & Schwarz, J.-O. 2015. Multi-scale characterization of porosity in Boom Clay (HADES-level, Mol, Belgium) using a combination of X-ray μ-CT, 2D BIB-SEM and FIB-SEM tomography. Microporous and Mesoporous Materials, 208, 1-20.
17. Keller, L. M., Schuetz, P., Erni, R., Rossell, M. D., Lucas, F., Gasser, P. & Holzer, L. 2013. Characterization of multi-scale microstructural features in Opalinus Clay. Microporous and Mesoporous Materials, 170, 83-94.
18. Ma, L., Dowey, P. J., Rutter, E., Taylor, K. G. & Lee, P. D. 2019. A novel upscaling procedure for characterising heterogeneous shale porosity from nanometer-to millimetre-scale in 3D. Energy, 181, 1285-1297.
19. Landis, E.N., Keane, D.T. 2010. X-ray microtomography. Materials Characterization 61, 1305-1316.
20. Teles, A.P., Lima, I. and Lopes, R. 2016. Rock porosity quantification by dual-energy X-ray computed micro-tomography. Micron, 83, pp. 72-78.
21. Ambrose, R.J., Hartman, R.C., Diaz-Campos, M., Akkutlu, I.Y. and Sondergeld, C.H. 2010. New pore-scale considerations for shale gas-in-place calculations. SPE-131772, paper presented at the Unconventional Gas Conference, SPE, Pittsburgh, PA, February 23-25.
22. Chalmers, G., Bustin, R.M. and Powers, I. 2009. A pore by any other name would be as small: the importance of meso-and microporosity in shale gas capacity. Presented at the American Association of Petroleum Geologists Annual Convention and Exhibition, Denver, Co, June 7-10.
23. Passey, Q.R., Bohacs, K.M., Esch, W.L., Klimentidis, R. and Sinha, S. 2010. Oil-prone source rock to gas-producing shale reservoir – Geologic and petrophysical characterization of unconventional shale-gas reservoirs. SPE-131350, paper presented at the CPS/SPE International Oil & Gas Conference and Exhibition in China, SPE, Beijing, China, June 8-10.
24. Goldstein, J., Newbury, D.E., Joy, D.C., Lyman, C.E., Echlin, P., Lifshin, E., Sawyer, L., Michael, J.R. 2003. Scanning Electron Microscopy and X-ray Microanalysis, 3rd edition. Springer, New York.
25. Wirth, R. 2004. Focused Ion Beam (FIB): A novel technology for advanced application of micro- and nanoanalysis in geosciences and applied mineralogy, 16 (6): 863-876.
26. Ishitani, T., Umemura, K., Ohnishi, T., Yaguchi, T., Kamino, T. 2004. Improvements in performance of focused ion beam cross-sectioning: aspects of ion–sample interaction. Electron Microscopy Journal, 53(5): 443–449.

27. Korfiatis, P., Skiadopoulos, S., Sakellaropoulos, P., Kalogeropoulou, C., Costaridou, L. 2007. Combining 2D wavelet edge highlighting and 3D thresholding for lung segmentation in thin-slice CT. British Journal of Radiology 80, 996-1004.
28. Li, B., Liu, R. and Jiang, Y. 2016. A multiple fractal model for estimating permeability of dual porosity media. Journal of Hydrology, 540, 659-669.
29. Stauber, M., Müller, R. 2008. Micro-computed tomography: a method for the non-destructive evaluation of the three-dimensional structure of biological specimens, Osteoporosis. Springer, pp. 273-292.
30. Buades, A., Coll, B., Morel, J.-M. 2005. A non-local algorithm for image denoising. Computer Vision and Pattern Recognition. CVPR 2005. IEEE Computer Society Conference on. IEEE, pp. 60-65.
31. Boruah, A. & Ganapathi, S. 2015. Microstructure and pore system analysis of Barren Measures shale of Raniganj field, India. Journal of Natural Gas Science and Engineering, 26, 427-437.
32. Saif, T., Lin, Q., Butcher, A. R., Bijeljic, B. & Blunt, M. J. 2017. Multi-scale multi-dimensional microstructure imaging of oil shale pyrolysis using X-ray micro-tomography, automated ultra-high resolution SEM, MAPS Mineralogy and FIB-SEM. Applied Energy, 202, 628-647.
33. Gundermann, T. & Odenbach, S. 2014. Investigation of the motion of particles in magnetorheological elastomers by X-µCT. Smart Materials and Structures, 23.
34. Iassonov, P., Gebrenegus, T., Tuller, M. 2009. Segmentation of x-ray computed tomography images of porous materials: a crucial step for characterization and quantitative analysis of pore structures. Water Resour. Res. 45, W09415. http:// dx.doi.org/10.1029/20 09WR0 08087
35. Heller, R., Vermylen, J., Zoback, M., 2014. Experimental investigation of matrix permeability of gas shales. AAPG Bull. 98, 975-995.
36. Javadpour, F., 2009. Nanopores and apparent permeability of gas flow in mudrocks (shales and siltstone). J. Can. Pet. Technol. 48, 16-21.
37. Glover, P.W.J. and Walker, E. 2009. Grain size to effective pore size transformation derived from an electro-kinetic theory. Geophysics, 74(1), E17-E29.
38. Johnson, D.L., Koplik, J. and Schwartz, L.M. 1986. New pore-size parameter characterizing transport in porous media: Physical Review Letters, 57(20), 2564–2567, http://dx.doi.org/10.1103/PhysRevLett.57.2564.
39. Glover P.W.J. (2015). Geophysical Properties of the Near Surface Earth: Electrical Properties, In: Gerald Schubert (editor-in-chief) Treatise on Geophysics, 2nd edition, Vol 11. Oxford: Elsevier, 89-137.
40. Glover P.W.J. (2010). A generalised Archie's law for n phases: Geophysics, 75(6), E247-E265, doi: 10.1190/1.3509781.
41. Revil, A., and Cathles, L.M. 1999. Permeability of shaly sands: Water Resources Research, 35(3), 651-662.
42. Ma, L., Slater, T., Dowey, P. J., Yue, S., Rutter, E. H., Taylor, K. G. & Lee, P. D. 2018. Hierarchical integration of porosity in shales. Sci Rep, 8, 11683.

43. Bahr, K. 1997. Electrical anisotropy and conductivity distribution functions of fractal random networks and of the crust: the scale effect of connectivity. Geophysical Journal International, 130(3), 649-660.
44. Nolte, D.D., Pyrak-Nolte, L.J. and Cook, N.G.W. 1989. The fractal geometry of flow paths in natural fractures in rock and the approach to percolation. Pure and Applied Geophysics PAGEOPH, 131(1-2), 111-138.
45. Ogilvie, S.R., Isakov, E. and Glover, P.W.J. 2006. Fluid flow through rough fractures in rocks: A new matching model for rough rock fractures. Earth and Planetary Science Letters, 604 241(3-4), 454-465.
46. Geng, L., Li, G., Zitha, P., Tian, S. and Sheng, M. 2016. A fractal permeability model for shale gas flow through heterogeneous matrix systems. Journal of Natural Gas Science and Engineering, 35, 593-604.
47. Glover, P. W. J. 2018. Modelling pH-Dependent and Microstructure-Dependent Streaming Potential Coefficient and Zeta Potential of Porous Sandstones. Transport in Porous Media, 124, 31-56.
48. Jennings, B. and Parslow, K. 1988. Particle Size Measurement: The Equivalent Spherical Diameter. Proceedings of the Royal Society of London. Series A, Mathematical and Physical Sciences, 419(1856), 137-149. Retrieved from http://www.jstor.org/stable/2398336
49. Peng, S., Yang, J., Xiao, X., Loucks, B., Ruppel, S.C. and Zhang, T. 2015. An Integrated Method for Upscaling Pore-Network Characterization and Permeability Estimation: Example from the Mississippian Barnett Shale. Transport in Porous Media, 109 (2), 359–376.